OPTIMIZATION AND QUANTIFICATION OF ERROR IN IMAGE CLASSIFICATION PIPELINES FOR NOISY SCIENTIFIC IMAGE DATASETS

Aritra Chowdhury

Submitted in Partial Fullfillment of the Requirements
for the Degree of

DOCTOR OF PHILOSOPHY

Examining committee:
Dr. Bulent Yener, Chair
Dr. Malik Magdon-Ismail
Dr. Charles V. Stewart
Dr. Alberto Santamaria-Pang

Department of Computer Science
Rensselaer Polytechnic Institute
Troy, New York

[August 2018]
Submitted June 2018

CONTENTS

LIST OF TABLES

LIST OF FIGURES

ACKNOWLEDGMENT

ABSTRACT

Image classification is an approach of pattern recognition in computer vision. The objective is to differentiate between different classes of images based on the quantification of contextual information in the images. Image classification is performed using data analytic pipelines. These pipelines are organized as interdependent and individual components. The components include image acquisition, image preprocessing, feature extraction, feature preprocessing, dimensionality reduction, learning algorithms. More steps may be added or removed from the pipeline. The quality of the image classification pipeline is measured by the validation error or test error in classification of unseen image instances that quantify the generalization error. Even though the error appears as a result of application of the learning algorithm, it is actually an accumulation of the errors introduced from different parts of the pipeline starting from the acquisition of the image from the sample, the feature preprocessing algorithms, the feature extraction algorithms and finally to the learning algorithm used for performing the classification. This error is propagated down the pipeline which finally accumulated in the form of the aforementioned classification error. In this thesis, we attempt to holistically, optimize, quantify and understand the contribution and propagation of error from the various components of image classification pipelines.

In the first part, we minimize the error in image classification pipelines. The first problem selected for demonstrating this is that of automatic microstructure recognition. The dataset for this problem is from the domain of material science. It consists of images of microstructures in the micrometer scale. We perform two classification tasks. The first task is of differentiating between dendritic and non-dendritic microstructures. The second task is for differentiating between longitudinal and transverse cross sections of microstructures. The objective for both the classification tasks is to find the best set of algorithms and hyper-parameters for minimizing the classification error. The approach used was an exhaustive grid search of the configuration space of algorithms and corresponding hyper-parameters for three stages of the pipeline - feature extraction, dimensionality reduction and learning algorithms. This exhaustive grid search is able to perform classification of the two tasks with a sufficiently high degree of accuracy. We demonstrate that pre-trained convolutional neural networks along with support vector machines with a linear kernel can be used for

characterizing microstructures. In addition, we also show that the exhaustive grid search based methodology can be used for finding the best algorithms and hyper-parameters for the problem of microstructure recognition in the domain of material science.

The second work involves an image classification problem in the domain of blood vessel characterization. The objective is to differentiate between vascular morphologies occurring in fluorescence microscopic 2D samples of neuropathological tissue samples. The main source of error in this problem arises as a result of imbalance in the training dataset. We address this problem by modeling artificial parametric 3D models of blood vessels to augment the training dataset and reduce the imbalance in the dataset. Pre-trained convolutional neural networks are used as the feature extraction algorithm in this work. We show that a combination of the artificial and natural data increases the accuracy of classification and as a result reduces the generalization error.

In the second part of the thesis, we try to understand the flow of error in image classification pipelines. The first work in this area involves the computation a score to quantify the quality of an image sample. This score is computed by leveraging the probabilities of machine learning algorithms. The dataset is annotated by a pathologist as *good* or *bad* depending on whether it has high or low amount of signal. Texture based features are used to extract information from the images. Classification algorithms are used to classify the data. We show that the probabilities of classification cluster into 3 groups of *good*, *bad* and *ugly*. This score therefore provides a way to filter a dataset based on the quality of the image samples.

The final work involves proposal of methods to quantify the contribution and propagation of errors in image classification pipelines. In particular, we describe an *agnostic* methodology to compute the contribution of errors from different components of the image classification pipeline. In addition, we also propose a model for quantifying the propagation of error along the pipeline. We show that algorithm selection and hyper-parameter optimization algorithms maybe used for error quantification. We empirically demonstrate that random search can efficiently quantify the contribution and propagation of error in in image classification pipelines.

CHAPTER 1
INTRODUCTION AND BACKGROUND

1.1 Overview

The goal of image classification or image recognition is to classify images based on contextual information present in the image. It i the task of assigning an input image a label from a fixed set of categories. Computer vision and machine learning based methods have been used to find solutions to this problem. Challenges in this problem consist of viewpoint variation, scale variation, rotation variation, inconsistent illumination and intra - class variation among others. More recently, deep learning methods known as convolutional neural networks have produced very good results on large scale image datasets. These datasets like Imagenet [1] consist of natural images consisting of multiple images objects that occur in everyday life. These images are from images in the scientific domain. Scientific images are usually imaged using sophisticated instruments like microscopes, MRI scanners, X-rays. In addition to the challenges in natural image classification, additional challenges in scientific images include data imbalance, noisy images, occlusion. In addition, the number of images in the dataset are usually small in number. As a result, image classification in the scientific domain comes with it's unique set of problems. Image classification systems in scientific domains are usually organized as pipelines or workflows. An example of such a workflow is shown in Fig. 1.1

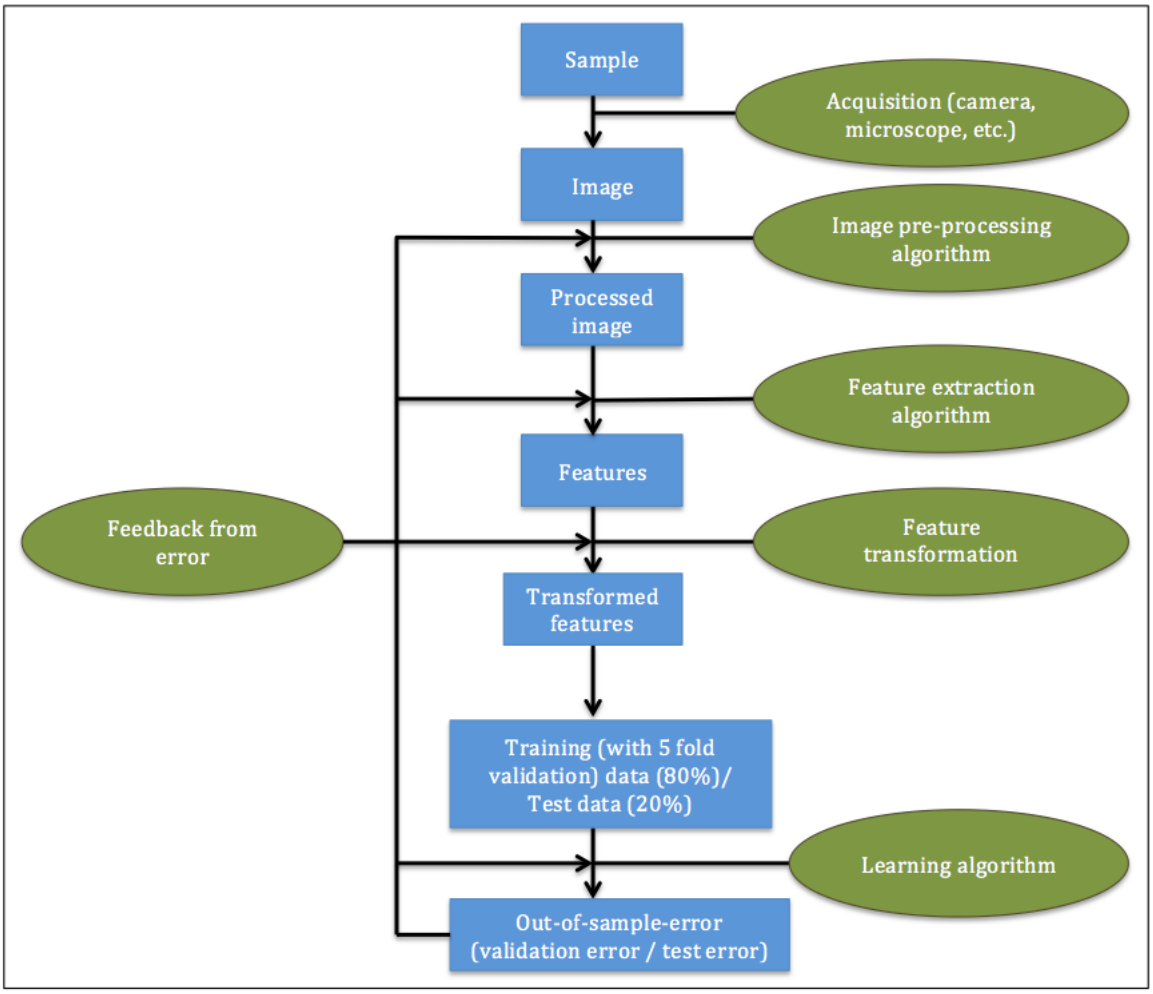

Fig. 1.1. Representation of an image classification pipeline

the flowchart starts with a sample that is imaged with acquisition technology like a camera or a microscope. The image is then processed using image pre-processing algorithms like normalization and standardization. This may also include image segmentation algorithms. This is followed by feature extraction algorithms that extract useful information from the images. Sometimes, the features extracted are transformed to a different vector space using feature transformation (feature selection or dimensionality reduction) algorithms. The dataset is then divided into training and test datasets in an 80-20 split. Finally, learning algorithms like random forests and logistic regression are used as learning algorithms to build a predictive model for the image classification problem. The performance of the pipeline is evaluated using classification metrics like cross-entropy loss, F1-score, accuracy, precision and recall. The error in the image classification pipeline maybe measured by such

metrics. In this thesis, we base our work on variations of this workflow. Even though the error in image classification pipelines are observed only in terms of the classification error, the source of the error is not just the classification algorithms. The final error is a result of the accumulation of error starting from the beginning of the pipeline right down to the learning algorithms used for classification. Therefore, attempts at improving the performance of image classification pipelines involve the use of better components in the workflow. This includes using better algorithms and methods for performing data analysis on the image datasets. It may also include improving the quality of the image dataset themselves. Another approach is to optimize and minimize the error from the pipeline by optimizing the data analytic portion of the pipeline as a whole. This could mean searching the solution space of algorithms to find the best set of algorithms for a particular problem. There is also a lack of interpretability of such image classification pipelines, in terms of understanding the source of the errors in the image classification pipeline pertaining to a particular dataset. In this thesis, we present approaches for minimizing the error in image classification with respect to scientific image datasets from different domains. These methods maybe used by domain experts or scientists to train high quality image classification pipelines for similar datasets. In addition, we also propose methods to quantify the error from all the components of a machine learning pipeline. These methods maybe used by domain experts and data scientists alike to understand and interpret results from image classification pipelines.

1.2 Contributions

We made the following contributions over the coarse of four projects discussed in the following chapters:

1. We perform an exhaustive search of data analytic algorithms in the problem of microstructure recognition. The steps included in this work include feature extraction, feature selection and classification algorithms. Each step consists of various algorithms. Two binary image classification tasks are performed in this work. They consist of classification between dendritic and non-dendritic microstructures and between logitudinal and transverse dendrites. We show that this methodology can be used to identify the best configuration of algorithms and hyperparameters in the domain of microstructure recognition. An exhaustive grid search on the pipeline also shows that pre-trained

convolutional neural networks maybe used to represent images of microstructures in the domain of material science

2. We report an automated method for characterization of microvessel morphology by performing data augmentation using parametric 3D models of neuropathological blood vessels. We show that a combination of natural and artificial data perform better in terms of classification metrics. We propose the development of parametric 3D models of blood vessels and this is used to augment datasets for two classification tasks that involve the classification of morphology of blood vessels. The consist of the classification between singular blood vessels and double blood vessels, and between vessels that consist of lumen and those that don't.

3. We propose a automated machine learning based score to quantify the quality of an image. This method maybe used to filter a dataset based on the quality of the images. This method can be used by domain experts to perform data analysis on a dataset that only consists of images with a high amount of signal.

4. We propose an *agnostic* methodology to quantify the contribution of errors from different components of an image classification pipeline. We show empirically that performing global random search on the entire pipeline maybe used for efficiently computing the statistics of error contribution from computational steps and algorithms in the image classification pipeline.

1.3 Outline

The following chapters detail our contributions with respect to optimization and quantification of error in image classification pipelines. In Chapter 2, we describe the problem of microstructure recognition with respect to two classification tasks. In Chapter 3, we propose the parametric 3D model based data augmentation method used in classification of morphologies of blood vessels in neuropathological tissue samples. In Chapter **??**, we present a machine learning based *Quality of Image* score that can automatically quantify whether the image is *good* or *bad*. In Chapter 5, we propose and describe a methodology to quantify the contributions of error from different components of an image classification pipeline. In Chapter 6 we present summarized conclusions and discuss relevant future work.

CHAPTER 2
IMAGE DRIVEN MACHINE LEARNING METHODS FOR MICROSTRUCTURE RECOGNITION

2.1 Introduction

Materials characterization is a critical aspect of the material design and discovery process. Recently, there has been much research in the field of materials informatics, a growing research area in which information technology and data science methods are used to interpret and analyze material data in order to accelerate the material discovery, design, and development process [2]–[6]. Currently, material design relies on chance discoveries and follows a classical synthesis-characterization-theory-computation approach [7]. Further, there is a heavy reliance on individual researcher background and experience which introduces significant bias and potentially error into the process of microstructure recognition, interpretation, and characterization. For example, quantification of microstructures traditionally is done using stereological measurements. Bias is introduced into stereological measurements through the requirement that an expert must first recognize and identify key microstructural features (inclusions, grains, or phases). This bias can be caused by a variety of factors, such as an individual's background, education, and experiences [7].

Although there have been recent advances in the field of quantitative microstructural science, there is still a heavy dependence on expert knowledge to identify what microstructural features are of interest for quantification [8]. Therefore it is desirable to expand upon work previously presented by DeCost and Holm in Reference [8], and further explore methods of quantitative microstructure representations which do not require *a priori* knowledge of microstructural features of interest or significance [7]. This work aims to leverage existing computer vision and machine learning techniques specifically for the challenge of microstructure recognition. While the overlap between computer vision, machine learning, and materials science is currently small [7], this work is a step towards increasing cross-disciplinary studies that challenge the current paradigm for microstructure characterization.

This chapter previously appeared as: A. Chowdhury, E. Kautz, B. Yener, and D. Lewis. "Image driven machine learning methods for microstructure recognition." *Computational Materials Science*, vol. 123 pp. 176-187, 2016.

Dendritic morphologies were chosen for this small case-study since dendrites are a well-characterized microstructural feature that exists in a variety of material systems (from single to multi-component). Size, shape, and spacing of dendrites vary depending on solidification behavior and chemistry, thus micrographs of this single feature can vary widely. The sample preparation and imaging methods used also contribute to the variety of micrographs produced from dendritic microstructures. Despite this variability in image data, it is still possible for human experts to look at a micrograph that contains dendrites and identify that it contains this microstructural feature, even though different orientations of dendrites (transverse or longitudinal) look distinctly different.

Computer vision and machine learning methods were applied to the task of identifying a particular microstructural feature of interest (dendrites) from micrographs that do not contain this particular feature (just as a human expert would identify that a micrograph contains dendrites). This recognition task is referred to in this work as Task 1. Task 1 is a high-level microstructure recognition task in the sense that dendrites are a type of microstructural feature that are not specific to a material system. A second classification task (referred to here as Task 2) was also completed, and involved distinguishing between longitudinal and transverse cross-sectional views of dendritic microstructures. This task may be viewed as a logical next step following the identification of dendrites in Task 1.

The contribution in this work is to investigate multiple computer vision and machine learning methods for microstructure recognition. We hypothesize that the approach and methods presented here can be generalized, and thus applied to a variety of microstructure recognition tasks that act as a necessary first step in characterization of a material system.

2.2 Alloy Fabrication and Sample Preparation

The alloy fabrication, processing, and metallographic sample preparation procedure followed to obtain images used in this work was based on the process detailed in References [9] and [10] and is summarized here.

A Materials Research Furnaces (MRF) three probe arc melter was used to fabricate alloys of varying Sn-Ag-Cu compositions. After melting alloys were allowed to solidify and were then prepared for directional solidification (DS). The solidified buttons were placed in a beaker on a hot plate. The button was re-melted while constantly being purged with Ar gas to minimize sample oxidation. The alloy melt was then transferred into a 4 mm

inner diameter quartz ampule with a mechanical pump. The rods were allowed to cool, then removed from the ampule, and placed in a larger quartz ampule (5 mm inner diameter) for DS. This ampule was then back-filled with Ar gas, sealed using a hydrogen torch, and inserted into the DS furnace.

DS was performed using a Bridgman-type apparatus in order to refine alloy microstructure. The tube furnace in this apparatus is a Thermolyne Type-21100 fitted with an Omega temperature controller. Following DS, alloys were removed from the quartz ampule, and small sections from the middle third of the rod were mounted in epoxy for metallographic sample preparation. Sections were mounted such that transverse and longitudinal orientations of β-Sn dendrites could be viewed. Samples were ground using silicon carbide (SiC) papers to 600 grit, then polished using 9, 3, and 1 μm diamond slurries. Colloidal silica was used as the final polishing step and as a chemical etchant so that the dendritic microstructure would be readily visible using light optical microscopy.

2.3 Image Data Sets

Image data used in this study includes micrographs taken over a span of approximately three years by students in the Lewis Research Group in the Materials Science and Engineering Department at Rensselaer Polytechnic Institute (RPI). All images taken by Lewis Research Group members are of solder alloys with dendritic microstructures. These alloys were manufactured, processed, and imaged at RPI, and a representative process of sample preparation was presented in Section 2.2. In order to supplement micrographs obtained at RPI, micrographs from the publicly available Dissemination of Information Technology for the Promotion of Materials Science (DoITPoMS) library [11] were used. Example images used in classification are provided in Figure 4.1.

Images were grouped into two data sets: Data Set 1 and Data Set 2, corresponding to classification Tasks 1 and 2 respectively. Data Set 1 is comprised of micrographs with and without dendritic morphologies. This data set includes all images with dendrites (longitudinal and transverse cross-sections) from both the Lewis Group and the DoITPoMS micrograph library [11]. All micrographs that do not depict dendritic morphologies were obtained from the DoITPoMS library. Data Set 1 includes 528 images that are each 227 by 227 square pixels. 264 original images were used in making Data Set 1 (132 micrographs containing dendrites and 132 micrographs without dendrites). Each original image is 270

by 500 pixels but includes a scale bar that interferes with feature extraction, therefore each image was cropped to yield two 227 by 227 square pixel images. Thus, 528 images were used for classification.

Data Set 2 is a subset of Data Set 1, and is comprised of micrographs that only contain dendrites, where each micrograph is either a transverse or longitudinal cross-sectional view. Micrographs used in this data set include both images from the Lewis Group and the DoITPoMS micrograph library. Data Set 2 contains a total of 188 images that are each 227 by 227 square pixels. As was done for Data Set 1, original images were cropped to remove the scale bar: 47 micrographs of each longitudinal and transverse sections (total of 94 original images) were cropped to create a 188 images used for classification.

2.4 Approach

The general approach applied to the task of micrograph classification involved feature extraction and feature selection (dimensionality reduction) to compute feature vectors that were then used for training, validating, and testing various classification models. The same approach was applied to both Data Sets 1 and 2 and is shown schematically in Figure 2.2.

Feature extraction is the first step in the process of classifying micrographs. Feature extraction starts with feature detection, where features in an image are local regions of pixels that include an 'interesting' part of a microstructure, such as a corner, edge, or blob-like object. Features detected using computer vision algorithms are not necessarily semantically meaningful, however are pixel patterns that are mathematically repeatable and recognizable, thereby making the region a good feature. Detected features are then described (or represented) in the form of a vector, called a feature vector. A feature vector is comprised of a set of detected features in the image, and each image can thus be described or represented by a feature vector. Multiple feature extraction methods were tested in this work in order to compare classification accuracies of different image representations.

These feature vectors, derived in the process of feature extraction, have high dimensionality and in this work feature selection was performed after feature extraction for computational efficiency and to preclude the curse of dimensionality . Feature selection involves reducing the length of the feature vector while still retaining image information. For ex-

The phrase 'curse of dimensionality' refers to issues associated with increasing data dimensionality in Euclidean space. Behavior of algorithms in low dimensional space, such as in three dimensions, may not generalize well to a higher dimensional space [12].

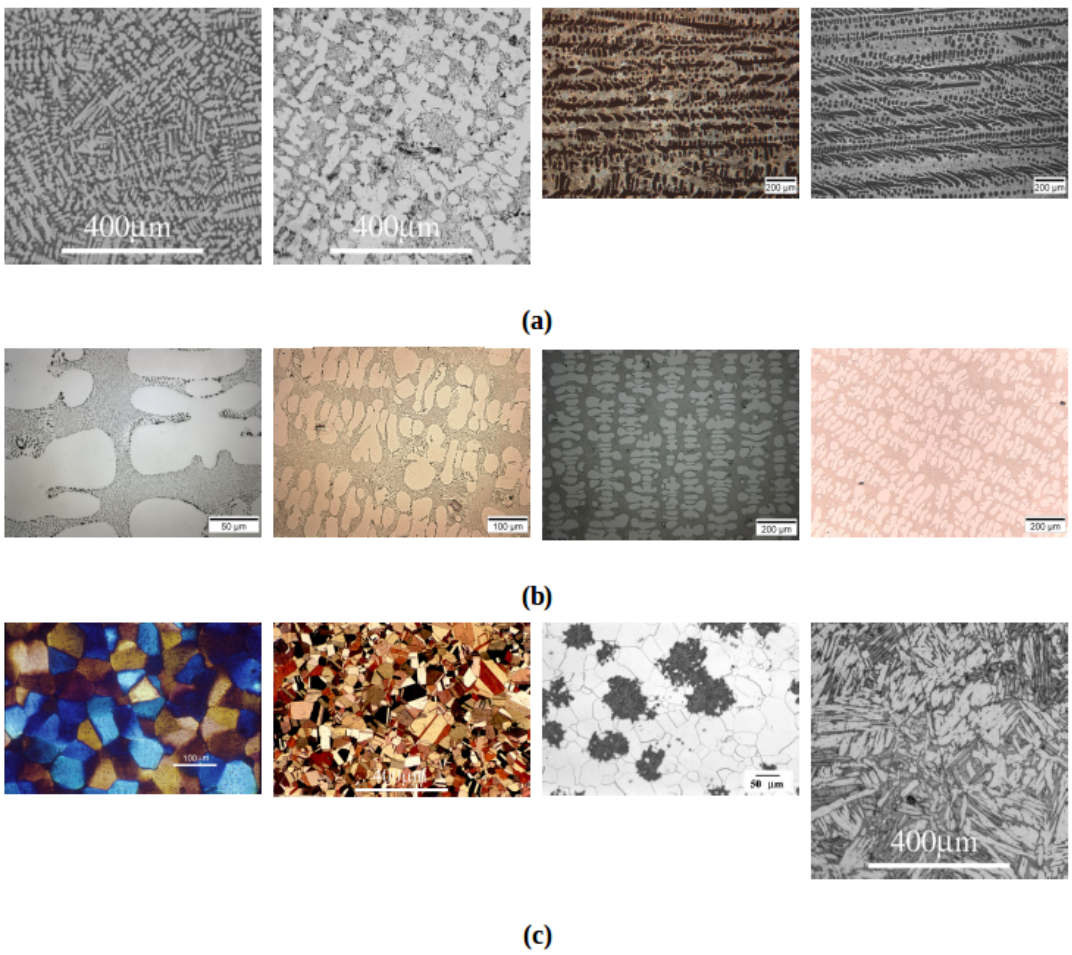

Fig. 2.1. Examples of micrographs used in classification. Micrographs shown in (a) and (b) are longitudinal and transverse cross-sectional views of dendrites, whereas micrographs in (c) do not contain dendrites. Micrographs in (a), (b) and (c) were used in Task 1, and micrographs in (a) and (b) were used in Task 2.

ample, if a feature vector is sparse, dimensionality reduction would involve reducing the sparsity of this vector. Different dimensionality reduction methods were applied to test how each technique impacted classification accuracies.

After feature extraction and selection, various classification models were trained, validated, and tested. A 5 fold cross validation split was used for each data set. This split was selected in order to minimize variance in model parameters, and to avoid over-fitting. These validation accuracies were then averaged and the standard deviation was calculated in order to evaluate model stability. We performed analysis on the two datasets (described in Section 2.3) in the form of two classification tasks: Task 1 and Task 2.

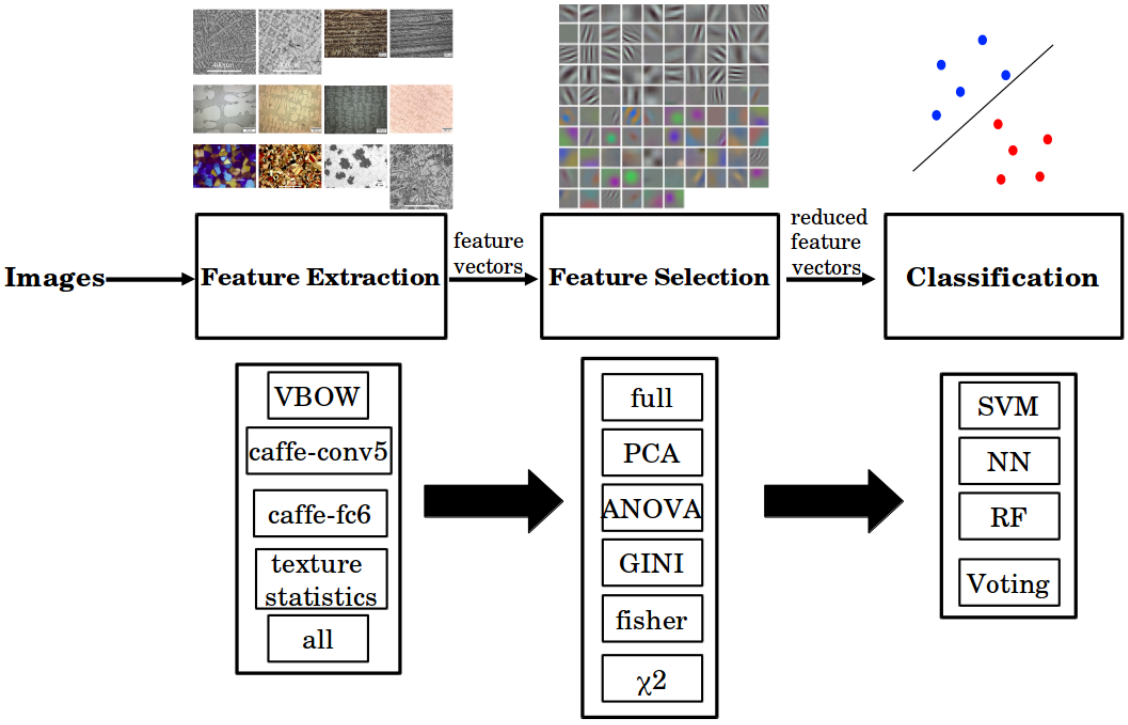

Fig. 2.2. Overview of approach used in classification of micrograph data. The approach summarized here shows 140 different combinations of feature extraction, feature selection and classification methods completed. The same approach presented here was completed first for Task 1 (Data Set 1), then for Task 2 (Data Set 2).

2.5 Computer Vision and Machine Learning Methods

As previously introduced in Section 2.4, multiple feature extraction and selection methods were tested with various classifiers in order to evaluate the best methods to apply to microstructure recognition tasks. The methods applied in this work are discussed in additional detail in Sections 2.5.1 - 2.5.3. Additionally, Section 2.5.4 provides a brief overview of computer vision and machine learning methods applied to other research in the field of materials science.

2.5.1 Feature extraction

Feature extraction methods applied in this work are texture and shape statistics (which include Haralick texture features [13], histogram of oriented gradients (HoG) [14], local binary patterns (LBP) [15], Hu moments [16], [17], Zernike Moments [18],threshold adjacency statistics [19]), visual bag of words (VBOW) [20], [21], and pre-trained convolutional neural

networks (CNN's). We used the publicly available Caffe framework [22] for all experiments involving pre-trained CNN's. The network was based on the architecture of Krizhevsky *et al.* for ImageNet [23]. The approach of using a pre-trained network was taken in this case-study because this is a good first step that does not require training to determine model parameters, which would be a difficult task with the small data sets used in this study [22].

Texture and shape statistics involve multiple feature extraction algorithms (previously listed) that operate on image texture and shape of objects within the image. These methods are introduced below:

Haralick features [13] are calculated using gray-level co-occurrence matrices (G_{ij}, shown below) which are square matrices of size N_g x N_g, where N_g is the number of gray levels in an image:

$$G_{ij} = \begin{bmatrix} p(1,1) & p(1,2) & \cdots & p(1,N_g) \\ p(2,1) & p(2,2) & \cdots & p(2,N_g) \\ \vdots & \vdots & \ddots & \vdots \\ p(N_g,1) & p(N_g,2) & \cdots & p(N_g,N_g) \end{bmatrix} \tag{2.1}$$

Each matrix element, $[i,j]$, is calculated by counting the number of times a pixel with value i is adjacent to pixel with value j. When considering a square pixel image, there are four directions for which a gray-level co-occurrence matrix can be calculated: horizontal, vertical, left diagonal, and right diagonal. Haralick texture statistics can be calculated based on the four gray-level co-occurrence matrices from each of these four directions. Haralick features thus describe the texture of an image. Fundamentally, texture is the arrangement of a certain feature or property, relative to the environment. In images, texture is the spatial distribution (arrangement) of gray-level variations in an image. Haralick features, computed from image gray-level co-occurrence matrices, capture texture patterns in an image.

The histogram of oriented gradients (HoG) [14] method describes an image with a set of histograms of gradient orientations from local regions of an image (referred to as cells). Each histogram reports the number of times a gradient orientation occurs in a given cell. In general, an image gradient is a two-vector that points in the direction of the greatest rate of change. The two components in the gradient vector include the gradient magnitude, $M(x,y)$, and the gradient orientation, $\alpha(x,y)$:

$$M(x,y) = \sqrt{g_x^2 + g_y^2} \tag{2.2}$$

$$\alpha(x,y) = \tan^{-1}(\frac{g_y}{g_x}) \tag{2.3}$$

where g_x and g_y are the x and y components of the gradient respectively. The normalized histograms of each cell are concatenated to form a descriptor vector for each image. The greater the number of bins, the more detailed the histogram, and thus feature vector.

Local Binary Patterns (LBP) [15] method also describes the texture of an image. Each image is split into cells and the neighborhood of each pixel (in each cell) is thresholded. The neighborhood surrounding each pixel is defined by the pixel's eight nearest neighbors. When the center pixel intensity value is greater than its neighbor, the pixel value is changed to 0, otherwise the pixel value is 1. For each pixel, an 8-digit binary number, which can be referred to here as a label, is created. A histogram is created for each cell that reports the frequency of each label. The histograms for each cell are normalized, then all histograms are concatenated to yield a feature vector for the entire image.

Hu moments [16], [17] are shape-based feature descriptors that describe, characterize, and quantify shapes of objects in an image. Hu moments are based on geometric moments, defined by $m_{p,q}(x,y)$:

$$m_{p,q}(x,y) = \int_{-\infty}^{\infty}\int_{-\infty}^{\infty} x^p y^q f(x,y)dxdy \tag{2.4}$$

Since images are a collection of pixels, the moment of an image must be expressed in terms of summations instead of integrals, as follows:

$$m_{p,q}(x,y) = \sum_{-\infty}^{\infty}\sum_{-\infty}^{\infty} x^p y^q f(x,y)dxdy \tag{2.5}$$

From the above equation, the area of an image would simply be defined by the 0th moment. The centroid of an image can also be defined using this concept of geometric

moments, as follows:

$$(\overline{x}, \overline{y}) = (\frac{m_{10}}{m_{00}}, \frac{m_{01}}{m_{00}}) \tag{2.6}$$

When moments are taken with respect to an image centroid, the moments are translation invariant, therefore a geometric moment can be defined relative to the centroid by $\mu_{p,q}(x, y)$:

$$\mu_{p,q}(x, y) = \sum_{-\infty}^{\infty} \sum_{-\infty}^{\infty} (x - \overline{x})^p (y - \overline{y})^q f(x, y) dx dy \tag{2.7}$$

Hu derived seven moment invariants from the geometric moment equation, $\mu_{p,q}(x, y)$, that are invariant to scale, translation, and in-plane rotation and can be computed from a binary image.

In order to compute Hu moments, a binary image must be used. A binary image was generated from the gray scale input images, by thresholding each image using Otsu's adaptive threshold algorithm [17], which is a global thresholding method that selects the optimal threshold value based on the image histogram. Otsu's algorithm assumes the gray scale intensities of an image follow a bi-modal distribution with two classes, and the threshold value is selected to maximize the inter-class variance. Hu moments were computed based on connected components of pixels in the binary image.

Zernike moments [18] are similar to Hu moments in that they describe the shape of objects in an image. An important difference between Hu and Zernike moments is that Zernike polynomials are orthogonal basis functions for Zernike moments. The use of orthogonal polynomials makes Zernike moments rotation invariant, and more robust to noise and minor variations in shape than Hu moments. Zernike moments are also calculated from a thresholded (binary) image.

Threshold adjacency statistics [19] are calculated from thresholded binary images. Three different binary images are generated from the original, using three different threshold values. For each white pixel in an image, the number of neighboring white pixels is counted [24]. The first statistic is the number of white pixels with no white neighbors. The second statistic is the number of white pixels with one white neighbor. The number of white

pixels with white pixel neighbors up to eight is counted (where there are eight nearest neighbor for each pixel in an image). Such statistics can be combined to create a feature vector that is subsequently used to distinguish and classify images.

All texture and shape statistics used in feature extraction (Haralick texture features, HoG, LBP, Hu and Zernike moments, and threshold adjacency statistics) were used to create a 1,775 dimensional feature vector for each image that represents texture and shape of objects within the image.

In addition to texture and shape statistics, Visual Bag of Words (VBOW) [20], [21] was also used for feature extraction. The VBOW technqiue is inspired from the 'bag of words' method used in document classification, where documents are considered as unordered sets of words. The corresponding words in the domain of image processing are local image features. These word descriptors are constructed around key points located by the Speeded Up Robust Features (SURF) [21] key points detection algorithm. These key points are extracted at regular locations at different scales making them very robust. The key point descriptors are categorized using a vector quantization technique such as k-means. The output of this discretization is a dictionary. Each image can therefore be encoded in the form of a histogram. This is done by extracting feature descriptors from the image, followed by finding the corresponding words to which the key points correspond to in the dictionary. The VBOW representation produced a 100-dimensional feature vector which was the pre-selected vocabulary size of the model.

A pre-trained convolutional neural network (CNN) model (trained on the Imagenet database) was also used in feature extraction. The ImageNet database contains 1.2 million images with 1000 categories. Here, the fifth and sixth layers of the pre-trained neural network were extracted and then used as feature descriptors for micrographs. The sizes of the feature representation obtained from the pre-trained ImageNet model were 43,264 and 4,096 for the fifth layer (caffe-conv5) and sixth layer (caffe-fc6) respectively.

Thus, for each image a feature vector was computed using each method described above. Concatenation of all computed feature vectors yielded a single vector which is referred to as "all" in Section 2.8. Feature selection (dimensionality reduction) and classification was then performed using feature vectors from each method and the combined (concatenated) feature vector.

2.5.2 Dimensionality reduction

Most of the image descriptors obtained from feature extraction methods lie in a high dimensional space (e.g. 1 x 43,264 for caffe-conv5). Therefore it becomes necessary to employ dimensionality reduction techniques to bypass the curse of dimensionality [25], and to improve computational efficiency. The process of reducing feature vector dimensionality is called dimensionality reduction, or feature selection. Six different dimensionality reduction techniques were tested in this work: principle component analysis (PCA) [26], ANOVA F-statistic (ANOVA) [27], χ^2 method [28], Fisher score [29], and Gini index [30]. A brief description of each method is provided in this section.

Principle component analysis (PCA) [26] is a feature transformation technique that uses orthogonal transformation to convert a set of observations of correlated variables to linearly uncorrelated ones. These orthogonal components are called principal components. In our work, we use only those principal components which account for 95 % of the variance in the data. PCA can be thought of as a transformation that reveals the structure of the data in a way that best explains the variance in the data. The drawback of this technique is that the features obtained after reduction are linear combinations of the original feature variables which occupy a different vector space than the original variables.

In addition to PCA, the Analysis of Variance (ANOVA) F-statistic [27] was used in feature selection. A one-way ANOVA F-test tests whether or not the different classes of the response variable have the same mean as the predictor variables. The p-value is calculated based on the F-statistic. These scores are then sorted in descending order and the features corresponding to the 30^{th} percentile are selected for analysis.

The χ^2 test is used in statistics to test the independence of two events. In the domain of feature selection, it is used to test whether the occurrence of a particular variable and class are independent. The χ^2 scores are ranked and the scores corresponding highest scores within the 30^{th} percentile are selected.

The idea behind the Fisher score is to find a subset of features such that the distance between data points in different classes is as large as possible and the distance between data instances in the same class are as small as possible. We select the features that correspond to the 30^{th} percentile of the highest Fisher scores.

The Gini index [30] is an impurity splitting method, where impurity is calculated based on the probability that any sample belongs to a particular class. The minimum value of the

index is 0, indicating that all of the members of the set belong to the same class, allowing for maximum useful information to be obtained. The opposite is true of samples in the set that are equally distributed in each class. The 30^{th} percentile threshold is used for selecting the features corresponding to Gini index scores.

2.5.3 Classification

Classification was performed on Data Sets 1 and 2 using four different methods: support vector machine (SVM) [31], random forest (RF) [32], nearest neighbor (NN) [33], and voting [34]. SVM, NN, and Naive Bayes [35] models were used as components of the voting classifier. Multiple classification algorithms were tested in order to determine which is the most accurate for micrograph classification. The classifiers applied to this case study were selected as representative models that have proven to yield high classification accuracies in other application areas, such as email filtering, text classification and more [36].

Support vector machines (SVMs) [31] are discriminative (or margin based) classifiers. A SVM constructs a hyperplane in high dimensional space that may be used for classification. The hyperplane is selected such that the distance from it to the nearest data point on each side is maximized, referred to as the maximum margin hyperplane. We perform both linear and non-linear classification. We perform linear SVM classification on the original feature space and the non-linearity is introduced by the radial basis function (RBF) kernel for transforming data points to an infinite dimensional space. Our approach is to experiment with different learning algorithms. Therefore, we choose a representative algorithm from particular families of learning algorithms. The RBF kernel has proven to be a good representation for non-linear kernels. Linear SVM is referred to here as SVM-L, and non-linear SVM using a RBF is referred to as SVM-RBF.

In addition to SVMs, nearest neighbor (NN) [33] classifier (an instance based classifier) was tested. The NN classifier assigns a test instance to a class based on the majority vote among the classes of the k-nearest neighbors of the training instances to the test instance. In our analysis, we selected k using five-fold cross validation.

Random Forest (RF) classifiers [32], also used in this work, are comprised of multiple decision trees and are therefore ensemble-based classifiers. A decision tree is a classification model that consists of a series of questions about the attributes of a data set, answers (such as yes or no), and follow-up questions. This series of questions is organized in a hierarchical

manner and consists of edges that are connected to different types of nodes, including a root node, internal nodes, and leaf nodes. A root node has no incoming edges and zero or more outgoing edges. An internal node has one incoming edge and two or more outgoing edges. A leaf node (also referred to as a terminal node) has one incoming edge and no outgoing edges. Each leaf node is assigned a label, and all internal and root nodes are assigned test conditions. In order to perform classification using a decision tree model, a path is followed from root to terminal nodes. This process will involve applying different test conditions, obtaining an answer, and moving to another internal node, and repeating this general process until a leaf/terminal node is reached. The path followed in a decision tree model will yield a class label for a given data instance. Classification using RF is dependent on the prediction of class label from multiple decision trees. Each tree in the model gives a class label, and the RF chooses the class with the most votes among the decision trees. Similar to RF, the voting classifier [34] is also an ensemble-based classifier that is based on majority voting among various classification modules. With RF, the modules were decision trees, and in this work we perform voting among three independent algorithms: SVM-RBF, NN and Naive Bayes.

Naive Bayes is a classifier model that depends on the inherent distribution of the training data set, and is thus categorized as a generative classifier. The Naive Bayes classifier uses Bayes' probability model and a decision rule to predict class of a data instance, where in this work each data instance is an image.

Naive Bayes is a statistical classifier that uses the concept of posterior probability for classification of new data instances. Each new data instance is assigned the class label that has the highest posterior probability. For a given set of variables $X = x_1, x_2...x_d$, the posterior probability for event C_j is calculated from the set of possible outcomes, $C = c_1, c_2, ...c_d$, where the set of possible outcomes is all class labels. Bayes' rule defines posterior probability of a class label (the probability X belongs to C_j) as:

$$p(C_j|x_1, x_2, ...x_d) \propto p(x_1, x_2, ...x_d|C_j)p(C_j) \tag{2.8}$$

where $p(C_j|x_1, x_2, ...x_d)$ is the posterior probability of class label C_j. Posterior probability can be re-written, given that conditional probabilities of independent variables are

assumed to be statistically independent:

$$p(C_j|X) \propto \prod_{k=1}^{d} p(C_j)p(x_k|C_j) \tag{2.9}$$

Using the Naive Bayes classifier, the new data instance X is classified by the class label C_j that has the highest posterior probability. In addition to the probability model defined above, the maximum *a posteriori* decision rule is applied for classification, meaning the hypothesis that is most probable is selected as the class label.

Classification was completed using each of the methods detailed above, for the full data set in addition to the reduced data sets obtained by the different feature selection techniques detailed in Section 2.5.2. Model parameters were determined using five-fold cross-validation.

In order to determine model accuracy and stability, average classification accuracies and standard deviations were calculated for every possible combination of classification, feature extraction, and feature selection method used. Average classification accuracies were calculated by taking the average of 5 fold cross validation of the dataset. The parameters of each algorithm were selected using the training fold of each split. Therefore the parameters were selected using another 5 fold cross validation of the training set and the training set was re-trained using the best combination of the parameters and the test accuracy on the remaining validation fold was calculated. This was performed 5 times and the average and standard deviation of the 5-fold validation accuracies was calculated.

2.5.4 Related Work in Materials Science

The methods discussed here are well established in the computer vision and machine learning disciplines, however only a select few have been previously applied to materials science and engineering challenges. Shape descriptor methods, such as Hu moment invariants, have previously been used to quantitatively describe microstructures for subsequent classification [37]–[41]. Specific applications of Hu moments in the field of materials science include automated classification of precipitate shapes in a two-phase microstructure [40], classification of cast iron microstructures [37]–[39], and analysis of precipitate shapes in nickel-based superalloys [41].

Additionally, the Visual Bag of Words feature extraction method with a Support Vector

Machine classifier were used for multi-class classification of microstructures by DeCost and Holm [8], as previously mentioned in Section 2.1.

2.6 Selection of Model Parameters

Each algorithm involved in our experimentation has their own set of parameters. Some of the parameters are set *a priori* and some are tuned using 5-fold cross-validation. Since we used cross validation to set the parameters for each combination of feature extraction, feature selection and classifier, there is no specific setting for each individual parameter for the algorithm. This approach of using 5-fold cross-validation to set parameters generates results that are more robust and thus more accurate with respect to each particular combination of feature extraction, feature selection, and classifier. We do a grid search over the parameter space using 5-fold cross-validation to estimate the best setting of the different parameters. Such parameters include number of neighbors in the nearest neighbor classifier, the SVM margin parameter (C), the RBF kernel parameter (γ), the number of trees or estimators in the random forests classifier. The parameters found by cross-validation are presented in detail in the supplementary article to this paper.

We also set a number of parameters before the experiments are run to limit the number of parameters to tune using cross-validation.

Default values were used for other parameters. We set the parameters in the feature extraction algorithms because this would represent a consistent test bed for the thorough computational experimentation over the feature selection and classification algorithms.

2.7 Software and Hardware Specifications

All of our experimentation was carried out with Python version 2.7 with the help of various open-source libraries. The opencv, scipy, skimage, numpy, mahotas and caffe packages (compatible with the Python version used in this work) were used for feature extraction. The skfeature library was used for experimentation with the various feature selection algorithms. The sklearn package was used for the various learning algorithms.

The hardware used for experimentation was a 3.3 GHz 4 core Intel i5 CPU.

2.8 Results and Discussion

This section reports the results from applying multiple feature extraction, feature selection, and classification methods to the task of micrograph recognition. Performance comparisons between feature extraction, selection, and classification methods are presented in Sections 2.8.1 and 2.8.2. The success of different methods are compared based on the mean classification accuracies and standard deviations. Results are presented in the form of tables, where each table compares all possible combinations of the three modalities (i.e. feature extraction, feature selection, and classification) that yield the maximum classification accuracy. The tables presented here summarize a large set of results that are provided in a supplement to this article.

2.8.1 Task 1 - Dendritic versus non-dendritic microstructures

Table 2.1 reports the feature extraction methods that yielded maximum classification accuracies for each combination of feature selection and classifier tested. It is clear from Table 2.1 that caffe-fc6 was the most effective feature extraction method because the majority of the maximum classification accuracies in Table 2.1 were computed using feature vectors obtained using caffe-fc6. These results suggest that microstructure image data is represented well using pre-trained neural networks (a type of deep learning algorithm), and this feature extraction method generalizes well.

It is also important to note that caffe-fc6 was not re-trained on Data Sets 1 and 2 used in this case study. The pre-trained weights determined via training on the millions of natural images in the ImageNet database were used, which were successfully applied to feature extraction here. This result is significant because in using a pre-trained neural network, no large database (i.e. millions) of micrographs was needed. The use of the sixth layer (fully connected) from the Caffe network [22] for feature extraction (caffe-fc6) resulted in superior classification performance over other feature extraction methods such as VBOW and texture and shape statistics for Task 1.

It is suggested that caffe-fc6 produced higher classification accuracies overall than VBOW and texture and shape statistics for Task 1 based on the difference in image representations (in the form of feature vectors) between each method. Furthermore, caffe-fc6 provided a more accurate image representation than caffe-conv5 (the 5th convolution layer of the Caffe network). This result could be due to the fact that features extracted from the

sixth layer was more representative of the image dataset.

Table 2.1. Feature extraction methods and corresponding classification accuracies (in %), that contributed to the maximum classification accuracy for each combination of feature selection and classification method tested for Task 1.

	Classifier				
Feature Selection	**SVM-L**	**SVM-RBF**	**NN**	**RF**	**Voting**
Full	**caffe-fc6** 90.52 ± 4.9	**caffe-fc6** 90.52 ± 4.9	**caffe-fc6** 87.69 ± 4.69	**caffe-fc6** 87.88 ± 6.19	**caffe-fc6** 89.02 ± 5.54
PCA	**caffe-fc6** 89.03 ± 3.58	**caffe-fc6** 89.03 ± 3.58	**caffe-fc6** 89.96 ± 2.53	VBOW 87.88 ± 1.84	**caffe-fc6** 88.64 ± 3.09
ANOVA	**caffe-fc6** 90.91 ± 4.32	**caffe-fc6** 90.91 ± 4.32	**caffe-fc6** 87.31 ± 3.23	**caffe-fc6** 87.13 ± 5.35	**caffe-fc6** 91.85 ± 4.25
χ^2	**caffe-fc6** 90.54 ± 3.99	**caffe-fc6** 90.54 ± 3.99	**caffe-fc6** 87.3 ± 3.73	caffe-conv5 87.49 ± 4.5	**caffe-fc6** 90.53 ± 4.96
fisher	**caffe-fc6** 89.01 ± 5.82	**caffe-fc6** 89.01 ± 5.82	**caffe-fc6** 89.58 ± 5	texture-statistics 87.5 ± 6.1	texture-statistics 89.58 ± 5.76
GINI	texture-statistics 89.01 ± 4.05	texture-statistics 89.01 ± 4.05	**caffe-fc6** 89.39 ± 4.64	texture-statistics 87.5 ± 5.46	caffe-conv5 89.58 ± 6.32

Feature selection was also investigated in order to determine if there was an overall best method for dimensionality reduction, and results are provided in Table 2.2. From results presented here, there is no one feature selection method that provided maximum classification accuracies for the majority of feature extraction and classifier combinations tested. This result could be attributed to the variability in the micrographs that do not depict dendrites (in Data Set 1). The micrographs selected as depicting non-dendritic morphologies are not all from the same material system and there is no common microstructural feature amongst this class.

The results also show that the feature selection method is sensitive to the types of feature extraction techniques and classifier models applied. Therefore, choice of dimensionality reduction should depend on the methods used for classification and feature extraction.

Table 2.2. Feature selection methods and corresponding classification accuracies (in %), that contributed to the maximum classification accuracy for each combination of feature extraction and classification method tested for Task 1.

	Classifier				
Feature Extraction	**SVM-L**	**SVM-RBF**	**NN**	**RF**	**Voting**
VBOW	Full 86.93 ± 2.09	Full 86.93 ± 2.09	Full 84.45 ± 3.16	PCA 87.88 ± 1.84	Full 85.4 ± 3.53
caffe-fc6	ANOVA 90.91 ± 4.32	ANOVA 90.91 ± 4.32	PCA 89.96 ± 2.53	Full 87.88 ± 6.19	ANOVA 91.85 ± 4.25
caffe-conv5	ANOVA 89.96 ± 6.11	ANOVA 89.96 ± 6.11	ANOVA 85.04 ± 4.48	χ^2 87.49 ± 4.5	χ^2 90.15 ± 5.08
texture-statistics	χ^2 89.96 ± 5.37	χ^2 89.96 ± 5.37	fisher 89 ± 5.74	fisher 87.5 ± 6.1	χ^2 89.78 ± 4.82
combined	χ^2 89.96 ± 5.37	χ^2 89.96 ± 5.37	fisher 89 ± 5.74	GINI 86.74 ± 5.51	χ^2 89.78 ± 4.8

Performance comparisons of classification models were also done for Task 1, and results are provided in Table 2.3. Linear SVM (SVM-L) provides maximum classification accuracies for over 50% of the possible feature extraction and selection combinations, indicating that this model generalizes well. This result also demonstrates that the data is linearly separable and use of a Gaussian kernel is not necessary for Task 1.

Table 2.3. Classification methods that contributed to the maximum classification accuracy (in %) for each combination of feature extraction and feature selection method tested for Task 1.

	Feature Extraction				
Feature Selection	**VBOW**	**caffe-fc6**	**caffe-conv5**	**texture-statistics**	**combined**
Full	**SVM-L** 86.93 ± 2.09	**SVM-L** 90.52 ± 4.9	RF 87.12 ± 4.37	**SVM-L** 87.88 ± 3.98	**SVM-L** 87.88 ± 3.98
PCA	RF 87.88 ± 1.84	NN 89.96 ± 2.53	**SVM-L** 87.3 ± 4.43	**SVM-L** 88.64 ± 3.32	**SVM-L** 88.64 ± 3.32
ANOVA	RF 83.72 ± 1.99	Voting 91.85 ± 4.25	**SVM-L** 89.96 ± 6.11	**SVM-L** 89.78 ± 5.76	**SVM-L** 89.78 ± 5.76
χ^2	**SVM-L** 80.29 ± 3.58	**SVM-L** 90.54 ± 3.99	Voting 90.15 ± 5.08	**SVM-L** 89.96 ± 5.37	**SVM-L** 89.96 ± 5.37
fisher	**SVM-L** 78.4 ± 1.64	NN 89.58 ± 5	Voting 89.57 ± 6.5	Voting 89.58 ± 5.76	Voting 89.58 ± 5.76
GINI	Voting 77.82 ± 2.85	NN 89.39 ± 4.64	Voting 89.58 ± 6.32	**SVM-L** 89.01 ± 4.05	**SVM-L** 89.01 ± 4.05

The performance of the pipeline is also measured using the plot in Fig. 2.3. Here, we sort the configurations in descending order based on the mean of their classification accuracies and plot the top 20 configurations with their corresponding error bars (one standard deviation). We observe from this plot that there is a minor difference in the results with respect to top 20 configurations. However, we also observe that certain algorithms come up multiple times in the top 20 configurations. So, even though there isn't a clear *best* configuration that is significantly better than all configurations, we can clearly see that there are certain algorithms which are better than others in terms of their ranking in the sorted order of configurations. We quantify this further by representing in Table 2.4 the average rank of the algorithms with respect to their ranks in the sorted configurations.

We can see from results in Table 2.4 that caffe-fc6, χ^2 and SVM are the best algorithms in the corresponding steps of feature extraction, dimensionality reduction and classification. However, caffe-fc6 has a larger margin with respect to the second best algorithm than χ^2

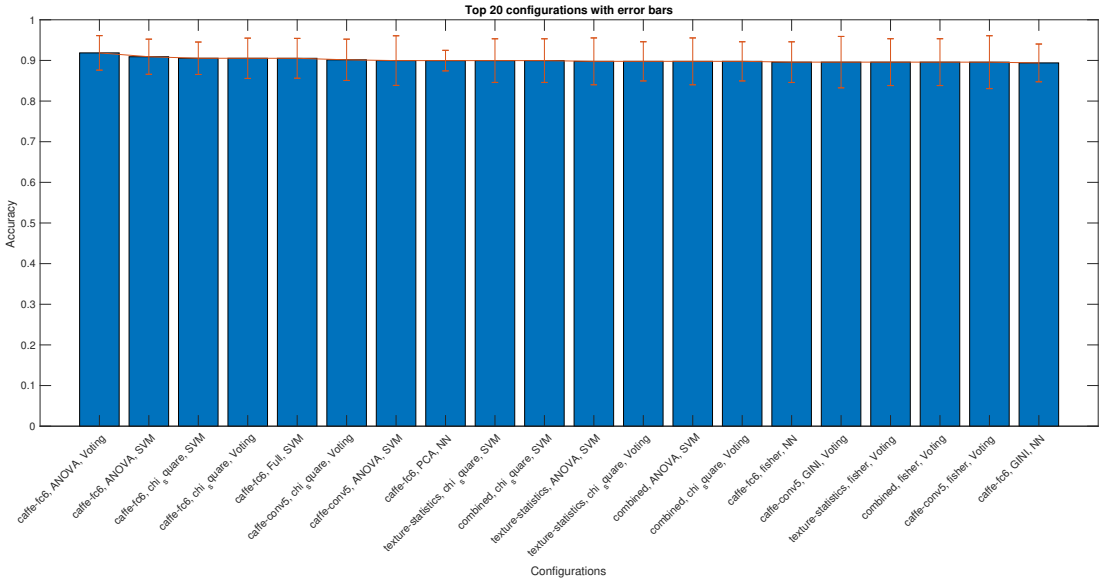

Fig. 2.3. Top 20 configurations of algorithms in Task 1 with error bars representing one standard deviation. There is no significant difference in the accuracies in the different configuations. Most of the feature extraction algorithms in the top 20 configurations are pre-trained CNNs (*caffe-fc6* or *caffe-conv5*)

and SVM in their respective steps. This indicates that caffe-fc6 is a good representation of the images for classification in Task 1.

2.8.2 Task 2 - Longitudinal versus transverse cross-sectional views of dendrites

Similar performance comparisons presented for Task 1 in Section 2.8.1 were also completed for Task 2 (longitudinal vs. transverse cross-sectional views of dendrites). A similar result was observed when feature extraction methods were evaluated, where caffe-fc6 represented micrographs well.

Again, features extracted using pre-trained neural networks dominates Table 2.5. This result shows that the features extracted from the sixth, fully connected layer in the Caffe network (caffe-fc6) have meaningful and distinguishable characteristics in terms of microstructural images. Although the majority of the maximum classification accuracies used features extracted via caffe-fc6, even higher values for classification accuracy were obtained using texture statistics and caffe-conv5 with a a linear SVM classifier. Classification accuracies obtained via SVM-L varied based on the feature selection method used, however the overall classification accuracies were highest for this classifier with features computed from either

Table 2.4. Average rank of the algorithms in Task 1 with respect to feature extraction, dimensionality reduction and classification. The average rank of an algorithm quantifies it's position in the sorted list of configurations.

Feature extraction	**Average rank**
caffe-fc6	47.82
texture-statistics	61.46
combined	64.46
caffe-conv5	72.39
VBOW	106.36
Dimensionality reduction	**Average rank**
χ^2	54.45
fisher	58.05
PCA	60.95
ANOVA	61.80
GINI	66.10
Full	66.55
Classification	**Average rank**
SVM	54.57
Voting	60.8
RF	81.40
NN	85.23

texture statistics or caffe-conv5. One major disadvantage of using texture statistics for feature extraction is that this method is a combination of multiple different feature detectors, and required prior knowledge of various techniques, that all perform differently depending on shape and texture of input data. The success of SVM as a classifier is subsequently discussed in additional detail.

Results from comparing feature extraction and classifier combinations indicate that in many cases feature selection did not improve calculated classification accuracies, as was seen in Task 1 results. This is shown in Table 2.6 by the majority of maximum classification accuracies computed using the full feature vector. When SVM-L was used for classification, feature selection methods improved results. The feature selection method used with SVM-L that yielded the maximum classification accuracy depended on the feature representation obtained in the feature extraction step. The same classification accuracies were obtained for each feature selection method, for a given feature extraction and classifier combination. In addition, the features extracted from the fifth layer (convolutional) in the pre-trained neural network perform poorly with respect to the other extraction methodologies. This can be

Table 2.5. Feature extraction methods and corresponding classification accuracies (in %), that contributed to the maximum classification accuracy for each combination of feature selection and classification method tested for Task 2.

	Classifier				
Feature Selection	**SVM-L**	**SVM-RBF**	**NN**	**RF**	**Voting**
Full	texture-statistics 95.79 ± 3.94	**caffe-fc6:** 95.74 ± 3.73	**caffe-fc6:** 94.49 ± 1.46	**caffe-fc6** 87.88 ± 1.64	**caffe-fc6:** 94.99 ± 2.38
PCA	texture-statistics 96.84 ± 3.07			VBOW 87.88 ± 2.95	
ANOVA	texture-statistics 97.37 ± 3.33			**caffe-fc6** 87.13 ± 1.64	
χ^2	caffe-conv5 96.78 ± 2.63			caffe-conv5 87.49 ± 15.69	
fisher	caffe-conv5 97.84 ± 2.65			texture-statistics 87.5 ± 8.25	
GINI	caffe-conv5 97.31 ± 2.42			texture-statistics 87.5 ± 8.25	

attributed to the fact that caffe-conv5 produces the feature representation with the highest dimensionality which is an order of magnitude greater than the second largest feature vector (caffe-fc6). Therefore, features extracted using caffe-conv5 are not robust (i.e. they have low accuracy with high standard deviation). Being lower in the network hierarchy of the CNN also means that the features may not be tuned properly to the task, and therefore features provide a less accurate image representation than features computed via caffe-fc6.

Table 2.6. Feature selection methods, and corresponding classification accuracies (in %), that contributed to the maximum classification accuracy for each combination of feature extraction and classification method tested for Task 2.

	Classifier				
Feature Extraction	**SVM-L**	**SVM-RBF**	**NN**	**RF**	**Voting**
VBOW	ANOVA 96.32 ± 2.68	**Full** 93.73 ± 3.96	**Full** 92.73 ± 3.91	PCA 87.88 ± 2.95	**Full** 93.98 ± 3.09
caffe-fc6	GINI 96.78 ± 2.63	**Full** 95.74 ± 3.73	**Full** 94.49 ± 1.46	**Full** 87.88 ± 1.64	**Full** 94.99 ± 2.38
caffe-conv5	fisher 97.84 ± 2.65	**Full** 84.46 ± 13.6	**Full** 77.19 ± 14.62	χ^2 87.49 ± 15.69	**Full** 78.45 ± 16.66
texture-statistics	ANOVA 97.37 ± 3.33	**Full** 93.23 ± 11.58	**Full** 94.24 ± 5.03	fisher 87.5 ± 8.25	**Full** 93.73 ± 11.09
combined	ANOVA 97.37 ± 3.33	**Full** 89.97 ± 9.08	**Full** 87.97 ± 9.02	GINI 86.74 ± 2.98	**Full** 84.46 ± 14.08

Lastly, classification models were evaluated for each combination of feature extraction

and feature selection with results presented in Table 2.7. SVM-L provided maximum accuracy with feature vectors calculated from the majority of feature extraction and selection methods. Linear SVMs again yield the majority of maximum classification accuracies in this table (similar to Table 2.1, which shows that this classifier has the most distinguishable capacity among the different models tested.

Table 2.7. Classification models that yielded the maximum classification accuracy (in %) for each combination of feature extraction and feature selection method tested for Task 2.

	Feature Extraction				
Feature Selection	**VBOW**	**caffe-fc6**	**caffe-conv5**	**texture-statistics**	**combined**
Full	**SVM-L** 95.26 ± 3.07	SVM-RBF 95.74 ± 3.73	**SVM-L** 88.57 ± 12.67	**SVM-L** 95.79 ± 3.94	**SVM-L** 95.79 ± 3.94
PCA	**SVM-L** 94.21 ± 3.07	**SVM-L** 96.29 ± 3.56	**SVM-L** 96.29 ± 2.09	**SVM-L** 96.84 ± 3.07	**SVM-L** 96.84 ± 3.07
ANOVA	**SVM-L** 96.32 ± 2.68	**SVM-L** 96.26 ± 3.19	**SVM-L** 91.9 ± 6.58	**SVM-L** 97.37 ± 3.33	**SVM-L** 97.37 ± 3.33
χ^2	**SVM-L** 94.74 ± 3.33	**SVM-L** 96.26 ± 3.19	**SVM-L** 96.78 ± 2.63	**SVM-L** 96.32 ± 3.16	**SVM-L** 96.32 ± 3.16
fisher	**SVM-L** 94.15 ± 1.03	SVM-RBF 95.74 ± 3.73	**SVM-L** 97.84 ± 2.65	**SVM-L** 96.29 ± 2.67	**SVM-L** 96.29 ± 2.67
GINI	Voting 93.98 ± 3.09	**SVM-L** 96.78 ± 2.63	**SVM-L** 97.31 ± 2.42	**SVM-L** 96.84 ± 3.07	**SVM-L** 96.84 ± 3.07

Results presented here demonstrate that certain combinations of methods (feature extraction, selection and classification) yield higher classification accuracies than others. The sixth fully connected layer in the Caffe network proved to represent micrograph data well for both tasks. The feature selection method for Task 1 depended on which classification model was used. For Task 2, the full feature vector yielded the maximum classification accuracies, thus feature selection did not appear to improve classification results for most classifiers tested. For classification models tested, linear SVM yielded the best results (highest accuracy) for both Tasks 1 and 2.

Similar to Fig. 2.3 for Task 1, we plot the top 20 configurations with respect to the mean of the classification accuracies for Task 2 in Fig. 2.4. Again, we observe the trend that there is no one clear *best* configuration. We again show the average rankings of the algorithms in their respective steps of feature extraction, dimensionality reduction and classification in Table 2.8.

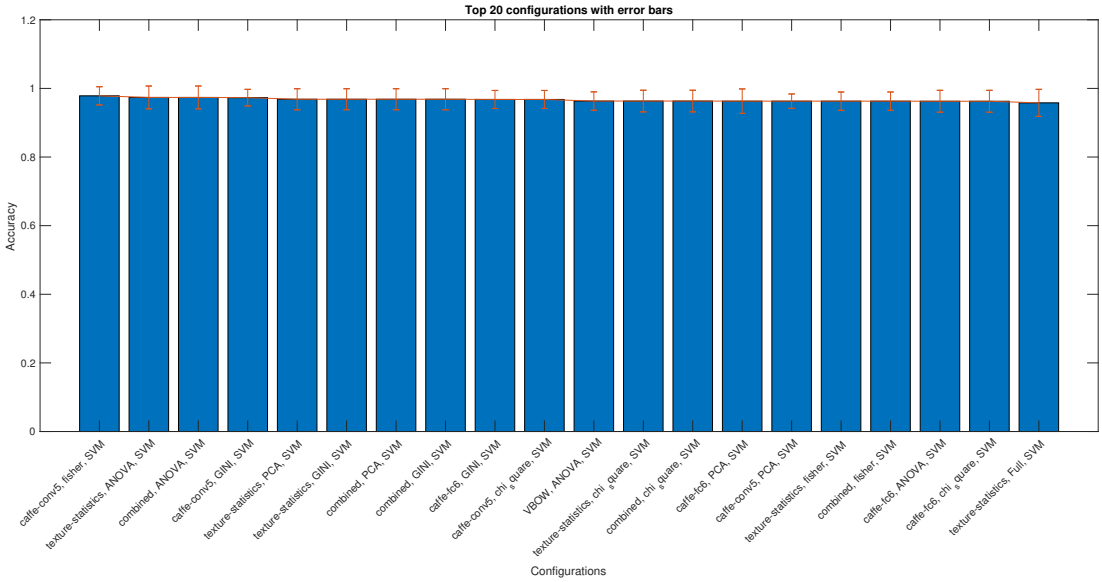

Fig. 2.4. Top 20 configurations of algorithms in Task 2 with error bars representing one standard deviation. There is no significant difference in the accuracies in the different configuations. Most of the feature extraction algorithms in the top 20 configurations are pre-trained CNNs (*caffe-fc6* or *caffe-conv5*)

From the results in Table 2.8, we observe that caffe-fc6, PCA and SVM are the highest ranked algorithms. We also note that in this case, the difference in rank between SVM and the next best classification algorithm (NN) is much greater than the corresponding differences in feature extraction and dimensionality reduction. This indicates that the SVM classification algorithm provides superior performance with respect to this task.

2.9 Limitations

In this work, pre-trained CNN's were used [23]. Training a convolutional neural network on the small amount of image data provided in Data Sets 1 and 2 (528 and 188 images, respectively) could prove difficult and potentially provide poor results in comparison to the results reported here. The reason for this is that deep neural networks require large image data sets for training because of their capacity to learn complex functions and are therefore prone to overfitting. The CNN used in this work was previously trained on millions of natural images, allowing for the model to generalize well to new data instances. Even though the original dataset that the neural network was trained on primarily consisted of natural images,

Table 2.8. Average rank of the algorithms in Task 2 with respect to feature extraction, dimensionality reduction and classification. The average rank of an algorithm quantifies it's position in the sorted list of configurations.

Feature extraction	**Average rank**
caffe-fc6	47.64
texture-statistics	58.64
VBOW	70.5
combined	81.82
caffe-conv5	93.89
Dimensionality reduction	**Average rank**
PCA	54.45
χ^2	58.05
ANOVA	61.80
GINI	66.10
fisher	66.55
Full	69.6
Classification	**Average rank**
SVM	31.22
NN	71.6
Voting	75.20
RF	103.97

we can see (from high classification accuracies) that the features extracted on micrographs provide meaningful representations.

There are an infinite number of potential material microstructures in the realm of materials science. Micrographs are two-dimensional images that represent a small sample of a three-dimensional microstructure, where 'microstructure' refers to material structure on a nanometer to centimeter length scale. Microstructures are formed from thermodynamic and kinetic processes, and depend on the crystal structure (atomic arrangement) of constituent elements. Although the elements on the periodic table are fixed, there are numerous combinations of these elements that can be processed and studied.

Let's first consider a material with a specific chemistry. There are various processes (annealing, quenching, cold working, etc.) that could yield a variety of microstructures. Additionally, the processed sample could be sectioned in different ways (transverse versus longitudinal, for example), again impacting the microstructure visible for subsequent analysis. There are also multiple imaging techniques available over a broad range of length scales (nanometer to centimeter). Images generated from different techniques have different con-

trast, brightness, and ranges of grayscale intensities or RGB levels. Expand this thought process to consider all possible material systems that can be generated from known elements with numerous imaging techniques (light optical microscopy, scanning electron microscopy, transmission electron microscopy, etc.). The possible microstructures we can analyze in the form of image data seems endless.

Therefore, the variety in micrographs used for materials characterization is vast, which is why expert knowledge and experience is relied on for such tasks as recognition, interpretation, and characterization. Training an algorithm to perform such classification/characterization tasks on diverse micrograph data sets is a challenge not only in organizing a data set for training, validation, and testing, but in obtaining reasonably good classification results (greater than random). The limitation presented here, is in the inherent variability of micrograph data, which could make classification tasks challenging, particularly if only a small data set is available for training and testing.

2.10 Conclusions

Computer vision and machine learning methods were successfully applied to the challenge of recognizing specific microstructural features of interest (e.g. dendrites) with varying magnifications, chemistries, and orientations. Two binary classification tasks were performed: classification between micrographs with and without dendrites (Task 1), and classification between longitudinal and transverse cross-sectional views of dendrites (Task 2). Data sets for Task 1 and Task 2 were 528 and 188 total images respectively. We are able to distinguish between microstructural images in terms of the presence of dendrites. A further refinement of the images can also be performed amongst the dendritic micrographs with respect to their cross-section, as shown in Figure **??**.

Feature extraction and dimensionality reduction techniques were utilized in order to represent micrographs in the form of feature vectors. Classification was then performed using support vector machines (linear and non-linear), voting, nearest neighbor, and random forest models. For each model, classification accuracy was calculated for full and reduced feature vectors, for each feature extraction and selection method tested.

Results demonstrated that pre-trained neural networks represented micrographs well, and required no previous knowledge of the nature of shapes or object within the images.

Furthermore, when pre-trained neural networks were used in feature extraction the highest classification accuracies for the majority of classifier and feature selection methods tested were achieved. Thus pre-trained neural networks generalize well. Maximum classification accuracies of 91.85 ± 4.25% and 97.37± 3.33% were obtained for Tasks 1 and 2 respectively. While computer vision and machine learning methods have previously been applied to microstructure image data [2], [8], [42]–[44], pre-trained deep neural networks have not yet been explored for this particular application, but have proven successful in other image recognition tasks [45].

Recognition of microstructural features traditionally requires expert knowledge of the particular material system under consideration. The image-driven machine learning approach to micrograph classification presented here challenges this paradigm.

2.11 Future Work

Neural networks are a promising feature extraction method for micrograph representation that could be further developed for application in more sophisticated characterization techniques, thereby eliminating the requirement of expert knowledge for recognition, interpretation, and characterization of microstructrural image data. Future work related to the exploratory study presented here, could involve application of pre-trained CNN's to more diverse micrograph data sets, or higher-level characterization tasks, such as average grain size measurement or calculating area fraction of a second phase. Furthermore, we would also like to incorporate deep learning algorithms on larger and more diverse micrograph classification tasks.

Acknowledgments

This work was is supported by the NSF under Grant #1056704 through the Metals and Metallic Nanostructures Program of the Division of Materials Research, and Grant #1302231 through the Information Integration and Informatics Program of the Division of Information and Intelligent Systems. The authors wish to acknowledge Mr. Jesse Werden and Dr. Jie Mao for some of the image data used in this work. Additionally, the authors thank the reviewers for providing thoughtful and thorough comments that contributed to the quality and clarity of the manuscript.

CHAPTER 3
BLOOD VESSEL CHARACTERIZATION USING VIRTUAL 3D MODELS AND CONVOLUTIONAL NEURAL NETWORKS IN FLUORESCENCE MICROSCOPY

3.1 Introduction

Characterizing the morphology of vasculature in digital pathology is an important step in defining the microenvironment within brain tissue samples. In particular, understanding the geometry of vessel configuration and its changes during a disease may provide deeper insight into the progression of neuropathological degenerative diseases such as Alzheimer?s disease. Images acquired using 20x object from immunofluorescent (IF) stained 6 um tissue sections with collagen IV antibody are used in this work. We attempt to characterize three different types of blood vessel morphologies which are found in relative abundance in our image data set. They are singular blood vessels with no visible lumen, singular blood vessels with a distinct lumen and blood vessels appearing as a pair; which we have named *RoundLumen-*, *RoundLumen+*, and *Twins* correspondingly. In this work, we show that it is possible to characterize blood vessels using convolutional neural networks (CNN) as opposed to traditional image processing techniques which involve segmentation and hand-crafted feature extraction. Instead, here we use pre-trained CNN to extract features from the images. This technique of ?deep transfer learning? is compared to the visual bag of words (VBW) method for feature extraction [46]. We conclude from the results that the features from pre-trained CNN are able to distinguish the morphologies of blood vessels better than the standard VBW method. Additionally, our work also shows that the construction of 3 dimensional (3D) virtual models of vasculature using parametric methods is a promising tool for dealing with infrequent scenarios in vascular analysis of brain tissue section. Acquisition of natural training samples is a time consuming and labor intensive process. Deep learning requires abundant training data for tuning the large number of parameters of the various

This chapter previously appeared as: A. Chowdhury, D. V. Dylov., Q. Li, M. MacDonald, D. E. Meyer, M. Marino and A. Santamaria-Pang, "Blood vessel characterization using virtual 3D models and convolutional neural networks in fluorescence microscopy" *IEEE International Symposium on Biomedical Imaging*, pp. 629-632, 2017

inherent models. If a certain class is imbalanced then the classification models could become prone to biased outcomes. The construction of 3D parametric models, presented here tackles these issues and creates a balanced high-fidelity classification model. In this study, we built a basic 3D vasculature model using our prior knowledge of blood vessel geometry, as guided by a pathologist. The 3D vasculature was repeatedly sliced at various angles and orientations to obtain 2D samples for training the machine learning model, thereby mimicking the physical sectioning of tissue during sample preparation for microscopy. In addition, a filtering technique was then used to fine-tune the virtual data to reflect the variability present in the naturally acquired samples. We train three models based on: virtual data, natural data and a mixture of both. The models are then tested on a reserved, independent portion of the naturally occurring data, with a hierarchical classification being performed to demonstrate a proof of concept. The first classification task involves distinguishing between singular blood vessels (*RoundLumen*) and pair of blood vessels (*Twins*). The second task of finer granularity is the classification between *RoundLumen-* and *RoundLumen+*. We report various metrics for both the classification tasks and observe that the artificial data improves upon the model trained from only the natural data. As far as we know, this is the first attempt to model vasculature using parametric 3D geometric methods exclusively. Statistical 2D and 3D shape models have been used extensively in medical image segmentation as detailed in [47]. However, these models use the training samples to statistically find a model of the object of interest. We do not generate virtual 2D models because we believe that we can obtain more variability in the training data by sectioning from the 3D models. Additionally, the 3D models may be extended to various other modalities in medical imaging.

3.2 Data

This section provides a detailed explanation of the different morphologies of blood vessels that are explored in this study. The first subsection is a description of the natural data curated from actual postmortem human tissue samples. The second subsection involves the description of the virtual 3D model of blood vessels which are used for generating samples for training the convolutional neural networks.

3.2.1 Natural data

FFPE Postmortem brain tissue samples from ten subjects with neurological disorders underwent sequential IF-multiplexing and fluorescent imaging. For each subject, approximately 25 images were acquired. This involves a cycling process of tissue section staining with 2-3 dye-labeled antibodies, imaging, dye inactivation and repeated staining with a new set of dye-labeled antibodies. Images underwent illumination correction, registration, stitching and auto-fluorescence subtraction. Collagen IV was used as a marker to detect all blood vessels. An image overlay is shown in Fig. 3.1.

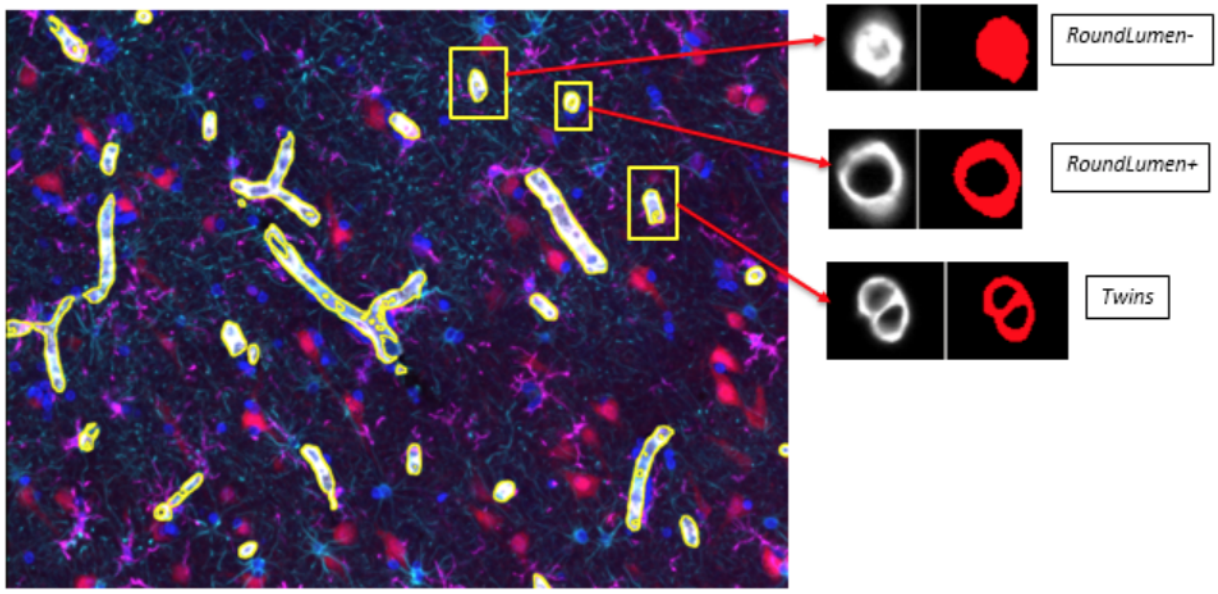

Fig. 3.1. Depiction of the different morphologies in the natural data with respect to a multichannel image, overlaid with different protein markers. The three types of morphologies analyzed in this study is represented on the right.

The number of instances of the three different types of morphologies are depicted in Table 3.1.

Table 3.1. Distribution of vascular morphologies

RoundLumen-	689
Roundlumen+	3427
Twins	266
Total	4382

3.2.2 Virtual data

The construction of the artificial model starts with defining a set of control points in three dimensional Cartesian coordinates. The control points reflect the basic structure that the blood vessel is supposed to represent. This is followed by interpolating between the points using a 3D cubic spline interpolator. This forms the skeleton or the center line that represents the center or the lumen of the blood vessel and is shown in Fig. 2(a). The 3D volume of the blood vessel is constructed after this step. We first define a number of parameters; the inner radius of the blood vessel (r); the outer radius (R). The number of sampling points along the spline (N); the number of sampling points in the radial direction (Nr). At each sampling point; we define a circular disk along the z-axis; by randomly perturbing the values of r and R. We also define an intensity model for the blood vessels depicted in Eq. 4.2. From the natural images, it seems that the intensity is high in the periphery of the blood vessel and decays towards the lumen and as we move away from the periphery. We model this using an exponential decay in the following form:

$$I(d) = I_{max} \exp(-\alpha |r\prime - d|) \tag{3.1}$$

where, I_{max} is the maximum intensity, is the calibration coefficient (in mm-1 units), $r\prime = (R + r)/2$. d is the distance from the center of the lumen. At each point on the disc, we define the voxel density as a normal distribution with mean $I(d)$ and standard deviation 0.01. This is followed by formulating the rotation matrix by calculating the angle between the tangent to the spline at that sampling point and the z-axis. The points corresponding to each point on the disc are therefore mapped or rotated along the curve by multiplying the coordinates with the rotation matrix. An example of this rotation is depicted in Fig. 3.2(b). We then discretize the coordinates such that we obtain an actual 3D image in the form of an array. This is depicted in Fig. 3.2(c). The intensity values are normalized and assigned to the corresponding discretized points in the 3-dimensional array. The volume rendered version of the 3D image is depicted in Fig. 3.2(d). Therefore, by changing the parameters of the model we can build several different 3D images and slice it at various angles to mimic the natural tissue cross sections at various depths and angles. Some examples the various models are depicted in Fig. 3.3.

The process of construction of the different types of morphologies in blood vessels is the

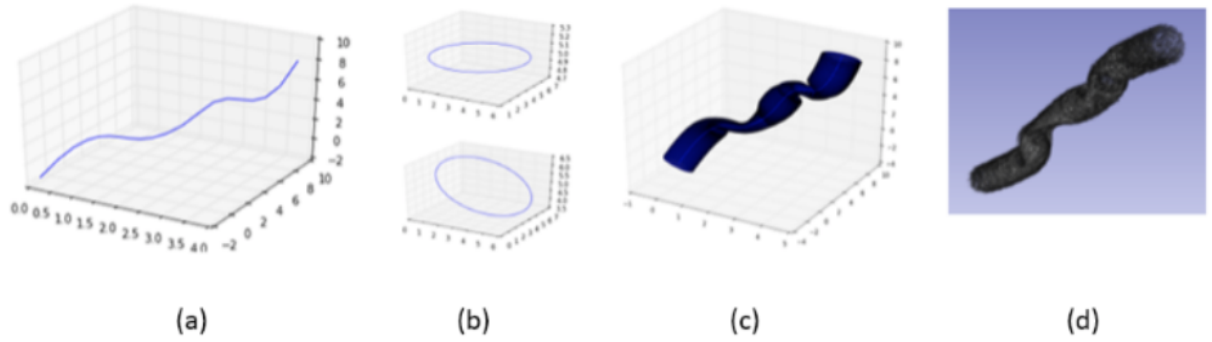

Fig. 3.2. Development of the 3D virtual model

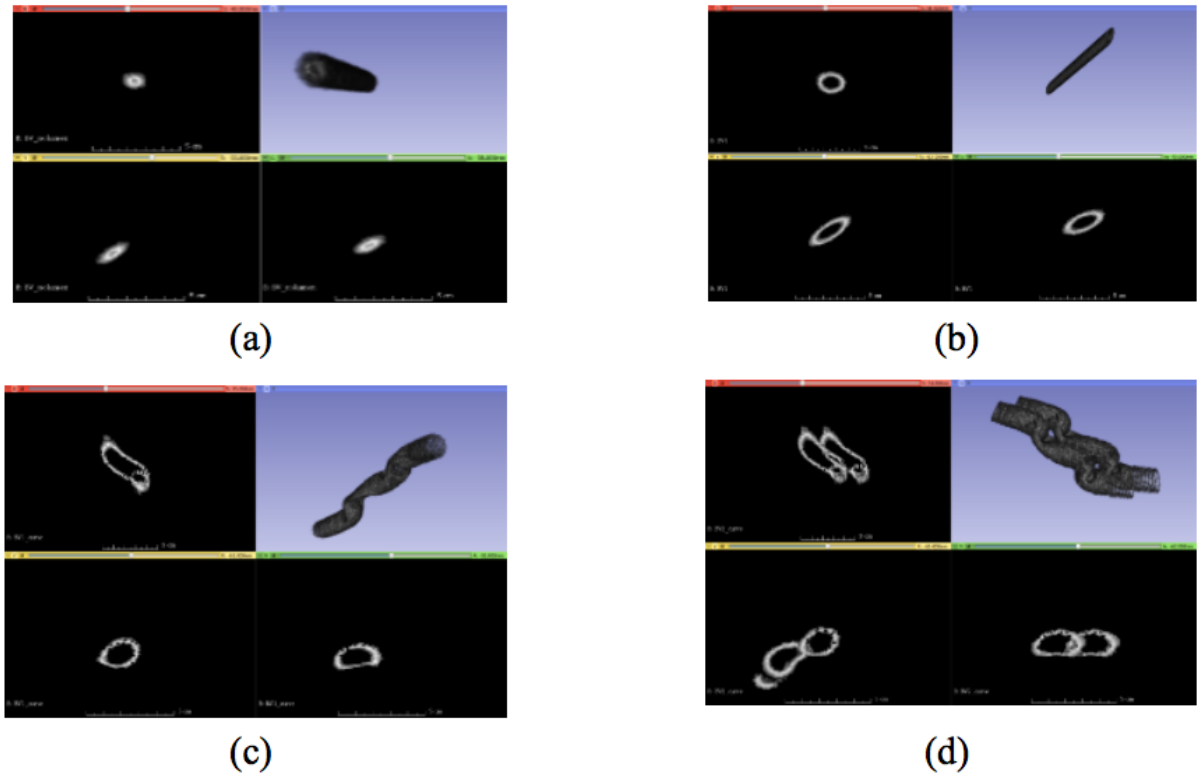

Fig. 3.3. 3D virtual models and their corresponding projections along different planes of view (a) Linear model of *RoundLumen-* (b) Linear model of *RoundLumen+* (c) Non-linear model of *RoundLumen+* (d) Non-linear model of *Twins*

same as that explained above. Fig. 3.3(a) is a blood vessel with a no lumen (*RoundLumen-*) and a linear skeleton. The control points are chosen such that they lie on the major diagonal of the unit cube; i.e. on the line x=y=z in Cartesian coordinates. Figures 3.3(b) and 3.3(c) are blood vessel with a single lumen having linear and non-linear structures respectively.

Fig. 3.3(d) is a model of a *Twin*. As we can see from the cross-sectional views, we obtain different types of morphologies that are similar to actual morphologies in the natural images. A very simple way of creating these multi-vessel structures is by perturbing or shifting the sampling points of the skeleton along a random direction. For example; to come up with a model of *RoundLumen-*, we simply set the inner radius r to 0. As shown in Fig. 3; the different morphologies that commonly occur naturally can be generated. As explained in the introduction; this serves as a viable alternative to using natural data for training convolutional networks.

3.3 Methods

A convolutional neural network is a type of artificial neural network in which are inspired by the organization of the animal visual cortex. CNNs consist of multiple neuron collections which process portions of the input image called receptive fields. The outputs are then tiled so that the input regions overlap and this in turn produces a better representation of the original image. This is what makes CNNs translation invariant. The CNN is made up of four types of layers: the input layer, the convolutional layer, the non-linear layer, the pooling layer; and the fully connected layer. The input layer is where the networks accept the images. The images consist of raw pixel values depicted by width, height and the number of channels. The convolutional layer will compute the output of the neurons that are connected to local regions in the input, each computing a dot product between their weights and a receptive field. The non-linear layer is the activation function responsible for introducing the non-linearity in the model. The various types of non-linear functions include the sigmoid, the tanh, and the rectified linear unit. The pooling layer performs a down sampling operation. The high-level reasoning in the neural network is done by fully connected layers. Their activations can be performed by simple matrix multiplication. In this work, we use the pre-trained convolutional neural networks as a feature extractor. This network consists of weights trained on the ImageNet dataset. We extract the 6th layer in the network which is a 4096-dimensional vector as a representation of the image. This may be considered as a transfer learning model because we transfer the weights learnt from another domain to blood vessel recognition. We use a pre-trained neural network called AlexNet [48] to extract features from the data.

We perform an experiment to show that pre-trained CNNs are efficient in representing

the vascular morphology. The experiment is performed on the natural data where 33 % of the data is held out as test data and the rest is used for training. Two models are developed. One of them uses the visual bag of words (VBW) [46] feature extraction method to extract the features; the other uses the AlexNet architecture to extract the features. A three-class classification (one vs rest) is performed using the logistic regression classifier. The accuracy, f1-score, precision and recall calculated on the same test data are reported for comparison.

Table 3.2. Comparison of feature extraction methodologies

Feature extractor	Accuracy	f1-score	Precision	Recall
AlexNet	91.92	91.93	91.98	91.92
VBW	78.38	77.38	76.71	78.38

The results in Table 3.2 show that pre-trained convolutional neural networks are a good choice for representation of vascular morphology.

3.4 Experiments and results

Features are extracted using the AlexNet architecture which is trained on the ImageNet [1] database. The weight parameters are used to extract the features in a feedforward manner. This is called transfer learning. 33 % of the natural data is held out as test data. All the experiments are performed on this dataset for maintaining consistency in the results. A filtering technique is introduced to appropriately extract slices from the 3D volumes. This is done by obtaining the probabilities of the artificial data using a model trained on the natural training data. The probabilities of the corresponding images are then sorted and the images with the highest probabilities are selected. This is a way to boost the artificial model. The filtered virtual data is then used to retrain the classifier. Examples of both the natural and artificial data are represented in the Fig. 3.4.

A hierarchical classification is performed to first classify the single blood vessels from blood vessels that bundled in pairs i.e *RoundLumen* vs *Twins*. The second classification task involves distinguishing between *RoundLumen-* and *RoundLumen+*. We perform three different types of training to demonstrate our proposed methods. The first type of training is done with only the naturally occurring data. The second type of training data consists only of the artificial data that has been filtered by the natural model as explained before. Finally, the third type consists of both the artificial and natural training samples. We refer to this as

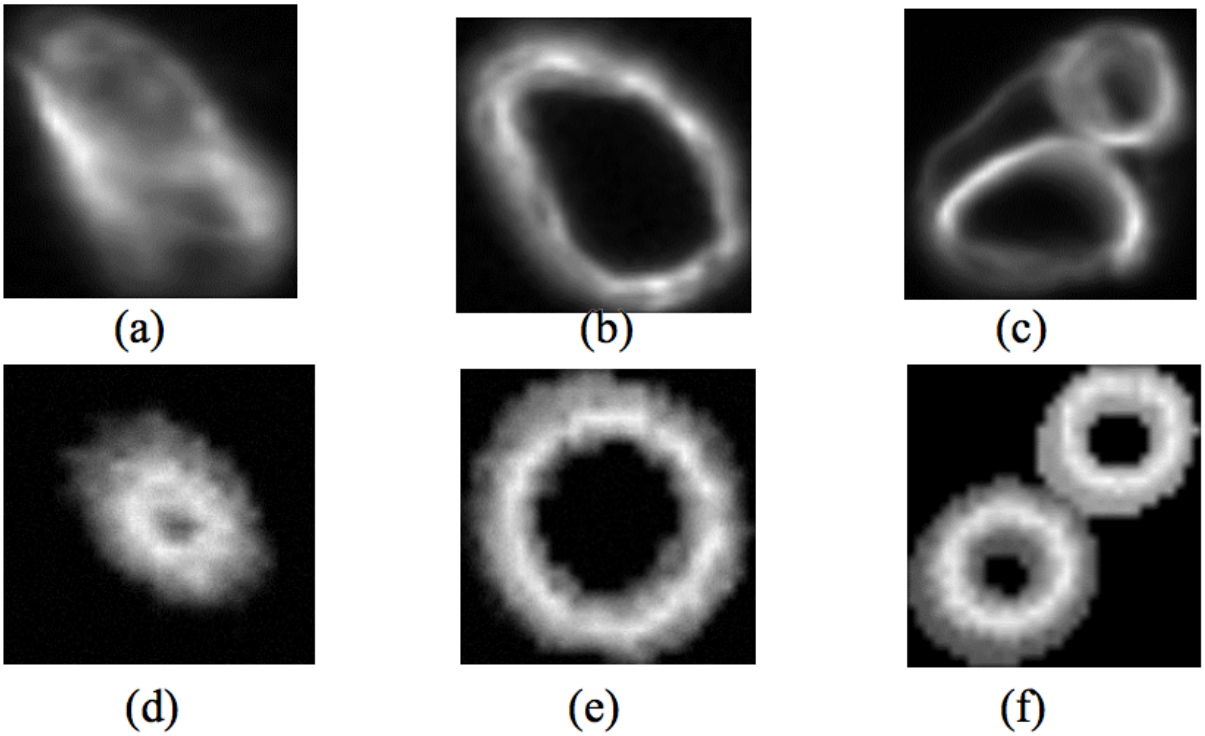

Fig. 3.4. Examples of vessel classes *RoundLumen-* (a/d), *RoundLumen+* (b/e) and *Twins* (c/f) for natural (a/b/c) and virtual data (d/e/f)

Mixed. All the results are reported on the held out 33 % of the natural data. The accuracy, f1-score, precision, recall and receiver operating characteristic (ROC), and precision-recall (PR) curves are reported in the following tables and figures for each of the two classification tasks.

Table 3.3. Results of binary classification between *RoundLumen* and *Twin*

Data	Accuracy	f1-score	Precision	Recall
Artificial	92.81	59.36	45.24	**86.36**
Natural	96.34	71.03	68.42	73.86
Mixed	**97.71**	**81.76**	**79.57**	84.01

Table 3.4. Results of binary classification between *RoundLumen-* and *RoundLumen+*

Data	Accuracy	f1-score	Precision	Recall
Artificial	98.38	99.02	99.38	98.67
Natural	96.34	71.03	68.42	73.86
Mixed	**98.60**	**99.16**	**99.29**	**99.03**

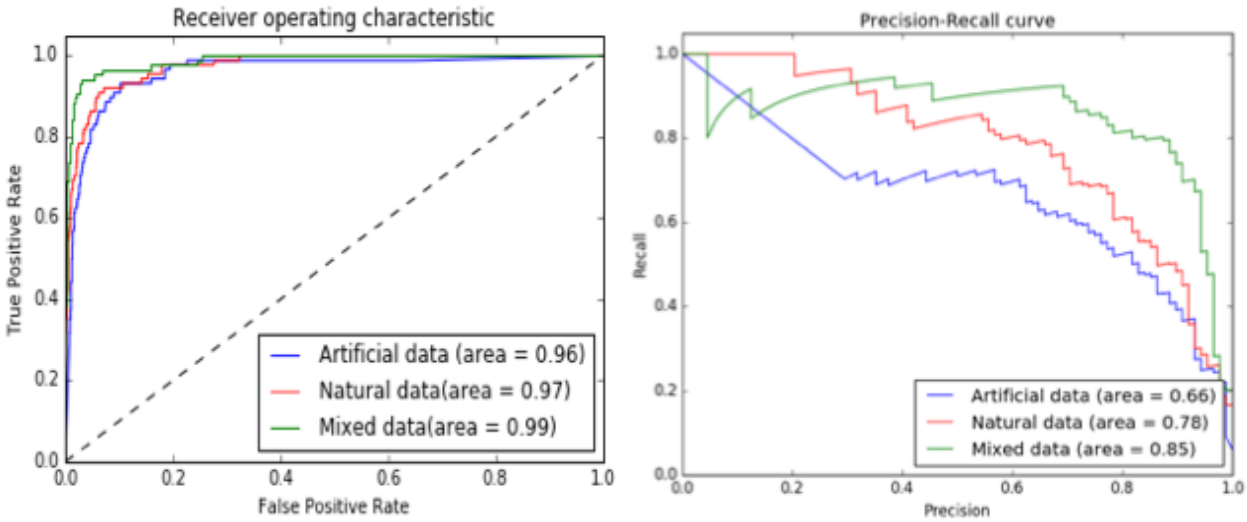

(a) ROC curve **(b) PR curve**

Fig. 3.5. Plots of the receiver operating characteristics (ROC) curve and the precision recall (PR) curve of the classification between *RoundLumen* and *Twins* along with the area under the curves (AUC) for the three experiments denoted as legends in the plots. From the nature of the curves, and the values of the AUC, we conclude that combining the using *mixed* data performs better than using the *Natural* data or the *Artificial data* in isolation.

The ROC and PR curves are calculated using the minority class in both the classification tasks, i.e. *Twins* for the first classification task and *RoundLumen*- for the second task. From Table 3.3, we can see that the artificial data captures the differences between the two classes. It is also able to identify *Twins*, which is the minority class in Task 1, from the high recall. Therefore, the results are boosted when we combine both the artificial and natural data. In addition, the ROC and PR curves in Figs. 3.5 confirms our hypothesis that virtual data may be used for building the models. The naturally trained model performs better than the virtual trained model. However, as we can see from the ROC curves, the model built from the mixed data improves the performance. Table 3.4 and Fig. 3.6 presents the corresponding results for the second classification task. In this case, we see that the virtual data performs better than the natural data and boosts the performance when trained on its own or in union with the natural data.

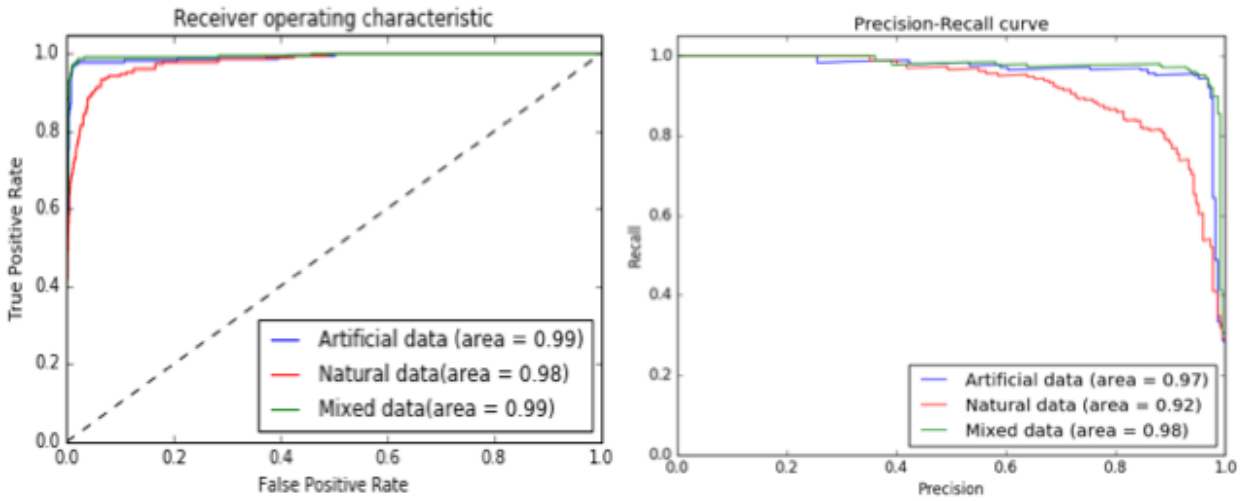

(a) ROC curve **(b) PR curve**

Fig. 3.6. Plots of the receiver operating characteristics (ROC) curve and the precision recall (PR) curve of the classification between *RoundLumen+* and *RoundLumen-* along with the area under the curves (AUC) for the three experiments denoted as legends in the plots. From the nature of the curves, and the values of the AUC, we conclude that combining the using *mixed* data performs better than using the *Natural* data or the *Artificial data* in isolation.

3.5 Conclusions

We have shown that the use of deep learning algorithms trained with a mixture of virtual and natural data results in a more accurate prediction of vasculature morphologies than the use of standard feature extraction methods (such as visual bag of words). The methodology of complementing natural data with synthetic samples holds potential for becoming a standard approach in deep learning with unbalanced datasets. In neuroscience, it could be applied to help elucidate the underlying mechanisms of common neurological degenerative diseases.

CHAPTER 4
A MACHINE LEARNING BASED APPROACH TO QUANTIFYING NOISE IN MEDICAL IMAGES

4.1 Introduction

As advances in medical imaging technology are resulting in significant growth of biomedical image data, new techniques are needed to automate the process of identifying images of low quality. Automation is needed because it is very time consuming for a domain expert such as a medical practitioner or a biologist to manually separate good images from bad ones. While there are plenty of de-noising algorithms in the literature, their focus is on designing filters which are necessary but not sufficient for determining how useful an image is to a domain expert. Thus a computational tool is needed to assign a score to each image based on its perceived quality. In this paper, we introduce a machine learning-based score and call it the *Quality of Image (QoI)* score. The *QoI* score is defined based on the probabilities of classification using the logistic regression classifier. We test our technique on clinical image data obtained from cancerous tissue samples. We used 723 tissue samples that are stained by three different markers (abbreviated as CK15, pck26, E_cad) leading to a total of 2,169 images. Our automated labeling is in agreement with the domain experts with an F1-score of 0.9044 on average. The results show a distribution of the *QoI* score for each of the three markers that correspond to the actual quality of the images from the marker according to the pathologist who labelled the images based on their perceived quality. We also quantify the quality of the markers and their differences based on the *QoI* scores of each sample stained using that marker. Furthermore, we propose a data-driven method by which images maybe recovered based on the *QoI* score and forwarded for further post-processing.

4.2 Data

The data we use is in the form of microscopic images. The colon cohort in this analysis was collected from the Clearview Cancer Institute of Huntsville Alabama from 1993 until

Parts of this chapter previously appeared as: A. Chowdhury, K. S. Aggour, S. M. Gustafson, B. Yener, "A Machine Learning Approach to Quantifying Noise in Medical Images." *Medical Imaging 2016: Digital Pathology*, vol. 9791, pp. 979110U, 2016.

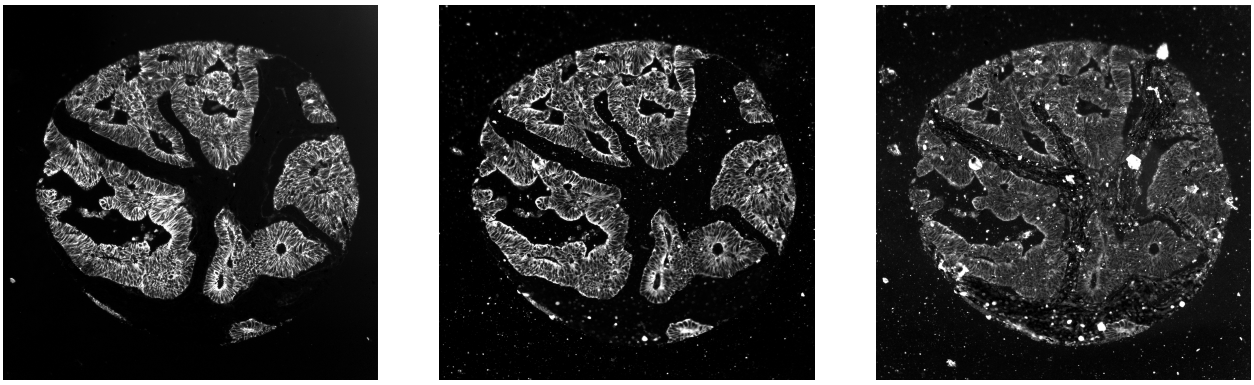

(a) E_cad **(b) pck26** **(c) CK15**

Fig. 4.1. Examples of a single colon tumor tissue sample stained with three different markers. E_cad is the least noisy with respect to undesirable artefacts, followed by pck26 and CK15 respectively.

2002, with 747 patient tumor samples collected as formalin-fixed paraffin-embedded specimens. The median follow-up time of patients in this cohort is 4.1 years, with a maximum of over ten years. Stage 2 patients comprise 38 % of this cohort, stage 1 and 2 combined are 65 % of the total patients. We have stained and processed 747 CRC subjects described above on tissue microarrays for 63 target proteins of consequence to cancer biology and ancillary image processing and analysis. A full description of materials and methods was described recently in [49]. The images in this work are stained with three different markers. The markers are Ecadherin (E_cad), pan-Keratin (pck26) and Keratin15 (CK15). The three markers stain epithelial cells in the tissue. The raw dataset consists of 747 tissue samples and each tissue sample has four images from each marker; resulting in a total of 2,988 images. 723 images from the 747 samples were selected by the pathologist for this work which result in a total of 2169 images from all the 3 stains. The images marked with E_cad have the least amount of noise associated with them. Images stained with pck26 is more noisy than E_cad, while CK15 is the noisiest among the 3 markers with respect to the presence of undesirable artifacts in the image. This difference in quality maybe observed from Fig. 4.1 from each of the 3 protein markers. We quantify the quality of both images and markers using the *QoI* score defined in this paper.

4.2.1 Feature extraction

We quantify the information in the three markers (E_cad, pck26, CK15) by texture features. Texture based features maybe used as a way to quantify the difference between

images based on amount of signal or noise in an image, and be able to distinguish between images of the types shown in Fig. 4.1 . These set of 13 features are based on gray-level intensity values, and texture information [50], [51] in the images. Haralick features [13] are calculated using gray-level co-occurrence matrices (G_{ij}, shown below) which are square matrices of size N_g x N_g, where N_g is the number of gray levels in an image:

$$G_{ij} = \begin{bmatrix} p(1,1) & p(1,2) & \cdots & p(1,N_g) \\ p(2,1) & p(2,2) & \cdots & p(2,N_g) \\ \vdots & \vdots & \ddots & \vdots \\ p(N_g,1) & p(N_g,2) & \cdots & p(N_g,N_g) \end{bmatrix} \tag{4.1}$$

Each matrix element, $[i, j]$, is calculated by counting the number of times a pixel with value i is adjacent to pixel with value j. When considering a square pixel image, there are four directions for which a gray-level co-occurrence matrix can be calculated: horizontal, vertical, left diagonal, and right diagonal. Haralick texture statistics can be calculated based on the four gray-level co-occurrence matrices from each of these four directions. Haralick features thus describe the texture of an image. Fundamentally, texture is the arrangement of a certain feature or property, relative to the environment. In images, texture is the spatial distribution (arrangement) of gray-level variations in an image. Haralick features, computed from image gray-level co-occurrence matrices, capture texture patterns in an image.

In addition to the features, labels are assigned to each image by domain experts based on the amount of noise in them. The label +1 is assigned if the image has some signal in it. This class is colloquially referred to as the *good* class. Images with a lot of noise in them where there is almost no signal are labelled as -1 or the *bad* class.

4.2.2 Data preprocessing

The three markers (CK15, pck26, E_cad) corresponding to each tissue sample are combined together to provide us with 723 x 3 = 2169 samples. We perform 5-fold cross validation on this data to compute the quality of image score and report the accuracy and F1-score on the validation data. The data is highly imbalanced. The ratio of bad to good images is roughly 1 : 18. Therefore, it is important to try to redress this imbalance. We use the synthetic minority oversampling technique (SMOTE) [52] on this data to perform oversampling. In this data balancing technique, the minority class (*bad*) is oversampled

by introducing synthetic samples along oining any or all of the k minority class nearest neighbors. Here k is set as 5. The number of neighbors from the k - nearest neighbors are randomly chosen depending on the amount of oversampling needed.

Principal components analysis (PCA) [53] is performed to reduce the number of features from 13 such that it captures 95 % of the information. This reduces the number of dimensions to 5. PCA is a feature transformation technique that uses orthogonal transformation to convert a set of observations of correlated variables to linearly uncorrelated ones. These orthogonal components are called principal components. PCA can be thought of as a transformation that reveals the structure of the data in a way that best explains the variance in the data. The drawback of this technique is that the features obtained after reduction are linear combinations of the original feature variables which occupy a different vector space than the original variables.

4.3 Methods and experiments

In this section, we describe the methods that we used in our analysis of the images and also show the results that we achieved from the application of these methods on our data.

4.3.1 Classification and analysis

The features from all the 3 markers are combined to form a feature matrix of size 2169 x 5 (after dimensionality reduction using PCA). We combine the data together for two reasons. The first reason is that this provides more samples for training. The second reason is that we want to create a quantity that quantifies the score over all the markers and is not just trained on one marker. We used the logistic regression classification algorithm for performing classification. We choose logistic regression algorithm because it is a simple classification algorithm that can make binary decisions. In addition, the sigmoid function used in logistic regression, squashes the the output of the linear function between 0 and 1. This value can be directly interpeted as a probability. This is exactly what we define as the QoI score in Eq. 4.2 defined in the next section. The F1-score for classification using the feature matrix on the binary classification problem is 0.9044 ($\pm$ 0.03 standard deviation). We use the F1-score instead of accuracy as the classification metric because of the imbalance in the dataset.

4.3.2 Quality of image score

The *Quality of Image (QoI)* score is defined as the probability that an image is from the *good* class. It is given by Eq. 4.2.

$$S_i \;=\; p_{i1} \tag{4.2}$$

A high value of the probability indicates that the image has high quality and must be used for further analysis. A low value of the probability denotes that the image belongs to the *bad* class and it can be discarded. An intermediate value of the probability is interesting because it denotes there is some signal in the image and that it may or may not be used for analysis. We denote such an image to be *ugly* which is neither *good* nor *bad*. The three sample images in the following figure show examples *good*, *bad* and *ugly* classes according to the QoI score.

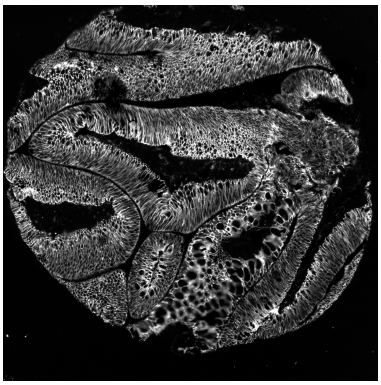

(a) A *good* image from E_cad marker with a *QoI* of 0.9945

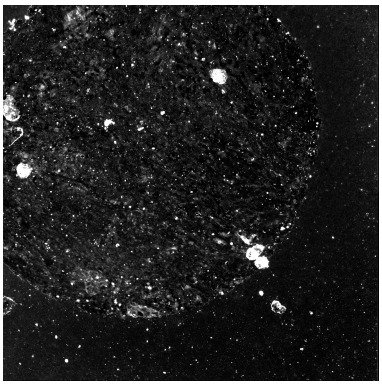

(b) A *bad* image from CK15 marker with a *QoI* of 0.0077

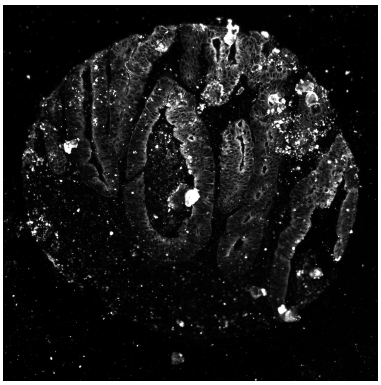

(c) A *ugly* image from pck26 marker with a *QoI* of 0.5262

Fig. 4.2. Examples of *good*, *bad* and *ugly* images based on the *QoI* score.

Fig. 4.2 shows examples of the images from the test data with their corresponding *QoI* scores. Fig 4.2a stained using the E_cad marker shows an image with a high *QoI* score. This image is clearly a *good* image as the tissue is easily observable and is not occluded. This image must be used for further analysis. Fig. 4.2b is an example of an image with a low *QoI* from the CK15 marker. This is image has literally no tissue and has regions of occlusions. This image should definitely be discarded. The third image in Fig. 4.2c from the pck26 marker, has some signal in it in terms of tissue but is also plagued with some noise. This is an example of what we call an *ugly* image and this sample may or may not be used in

further analyses.

4.3.3 Results and discussion

We plot the distribution of *QoI* scores in Fig. 4.3. Figs. 4.3a, 4.3b, 4.3c, 4.3d correspond to the distribution of the images from all markers, E_cad, CK15 and pck26 respectively.

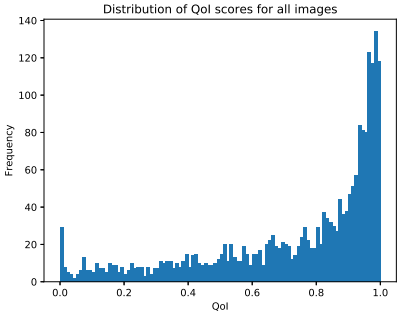

(a) Distribution of scores on all the images

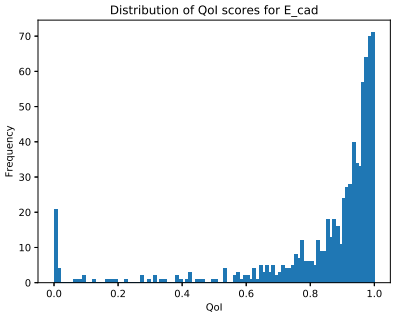

(b) Distribution of scores from E_cad marker.

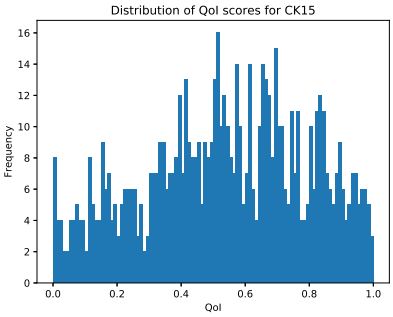

(c) Distribution of scores from CK15 marker.

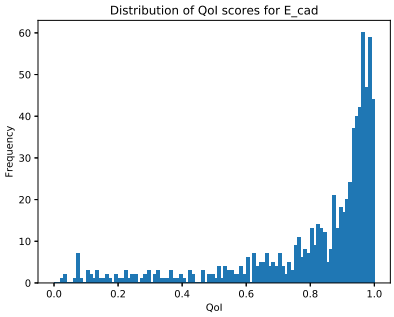

(d) Distribution of scores from pck26 marker

Fig. 4.3. Distribution of *QoI* scores on the images. According to the pathologist, the perceived quality of the images from the E_cad and pck26 marker is good and the images from the CK15 marker has low signal and high noise in general. This is reflected in the distribution of these markers

The pathologist who labelled the images as *good* or *bad* based on the perceived quality of the images claimed that the images from the CK15 marker has more noise than images from E_cad and *pck26*. This is exactly what we quantify using the *QoI* score. The ratios of *good* to *bad* images for E_cad, CK15 and pck26 are approximately 19:1, 19:1 and 17:1 respectively for the three markers. The difference in quality of the images are not captured by the distribution of the labels themselves. The distributions of the scores of the three markers in Fig. 4.3 clearly quantify this difference. We can see from Figs. 4.3b and 4.3d

that the *QoI* scores are scewed towards higher values close to one. On the other hand Fig. 4.3c shows that there are a large number of images that maybe denoted as *ugly*. The average values of the probabilities over all the images in a marker can be used to quantify the quality of the marker itself. In fact, the average values of the probabilities over all images in E_cad, pck26 and CK15 are 0.85, 0.54 and 0.82 respectively. Therefore, the quality of the markers E_cad and pck26 is better than that of CK15. We divide the range of the scores into 3 equally spaced regions to demonstrate the difference between the three markers in more detail. The three regions are *good* with a score range of 0.67 to 1, *bad* with a range of 0 to 0.33 and *ugly* with a range of 0.33 to 0.67. These values are chosen to demonstrate the differences between the markers. We discuss methods to select these thresholds later.

Table 4.1. Percentage of the number of images that fall in the *good*(0.67- 1), *bad* (0 - 0.33) and *ugly* (0.33 - 0.67)regions of the QoI score with respect to the 3 markers. The percentage values clearly quantify the claim that E_cad is the least noisy followed by pck26 and CK15.

Marker	**good** (%)	**bad** (%)	**ugly** (%)
E_cad	43.14	16.33	10.54
pck26	40.15	19.52	18.61
CK15	16.71	64.14	70.85

Let's focus on the region between the scores of 0.33 and 0.67, which we may denote as the *ugly* region of the *QoI* score in Table 4.1. The percentage of images from E_cad, pck26 and CK15 that fall in this region are 16.33 %, 19.52 % and 64.14 % respectively. These values also show that there are more contentious images with respect to the *QoI* score in CK15 than in E_cad and pck26. We also show the distribution of the scores over all the images in the three markers in Fig. 4.3a. The plot shows that most of the images have high quality. This is because images from E_cad and pck26 which have high amounts of signal (according to the pathologist) account for two-thirds of the total data. It is clear from the results that the *QoI* score maybe used to quantify the amount of usable signal in the image. The *QoI* of an image sample provides an indication as to whether a particular sample may or may not be used in the analysis.

There could be a number of different ways to use the *QoI* scores usefully for performing analysis. In Table 4.1, we selected the thresholds arbitrarily by dividing the range of the scores into 3 equally spaced regions - *good*, *bad* and *ugly*. A threshold maybe set on the QoI by the analyst and only those images above the threshold can be used for further analysis.

Alternatively, a data-driven approach maybe used to leverage the *QoI* score for performing further analysis. For example, the next step of the process maybe to classify the images into different grades of cancer. In this step the *QoI* score can be obtained for the dataset in question. The classification maybe started with a sample of images that have *QoI* above a certain threshold. Then images are added to the training in batches based on the *QoI* scores in a sequential manner. This procedure maybe repeated until the accuracy on the held out test set plateaus or decreases. This threshold could be used as the cutoff *QoI* score to threshold the images for analysis. This is a way to not only use the good images, but also include the information from *ugly* images into the post-processing analyses.

4.4 Conclusions

We introduce in this paper a machine learning based score to quantify the perceived quality of an image. The score is defined as the confidence of a data point to be classified as *good* with respect to a classification algorithm, namely logistic regression . Images that have high or low information content are easy to label as good or bad respectively. A labeling of the ugly class becomes dependent on the observer. Therefore computing a score is a more natural way of extracting this third class of images. The score helps us retrieve images that may have been discarded by a simple binary classification; or that may have gone unnoticed by a human eye. This score maybe used by medical practitoners to not only quantify the quality of an image but also the quality of a protein marker as a whole, as we demonstrate in the experiments section. Thus, this score maybe used to filter a dataset by only using image samples and markers that have usable information in them. We propose a data-driven approach to select an appropriate threshold selecting scheme. This will not only help increase the overall quality of analysis, but also remove the burden on pathologists to manually filter and select *good* images from the dataset.

CHAPTER 5
ALGORITHM SELECTION AND HYPERPARAMETER OPTIMIZATION BASED QUANTIFICATION OF ERROR CONTRIBUTION IN IMAGE CLASSIFICATION PIPELINES

5.1 Introduction

Machine learning and data science has entered many domains of human effort in modern times. The number of self-reported data scientists has doubled in recent years [54]. They have entered various domains including academia, industry and business among others. There has therefore been a demand for machine learning tools that are flexible, powerful and most importantly interpretable. The effective application of machine learning tools unfortunately requires an expert understanding of the frameworks and algorithms that are present in a machine learning pipeline. It also requires knowledge of the problem domain and understanding of the assumptions used in the analysis. In order for these tools to be used adequately by non-experts; additional tools must be developed for understanding and interpreting the results of the application of a data analytic pipeline on a domain specific problem.

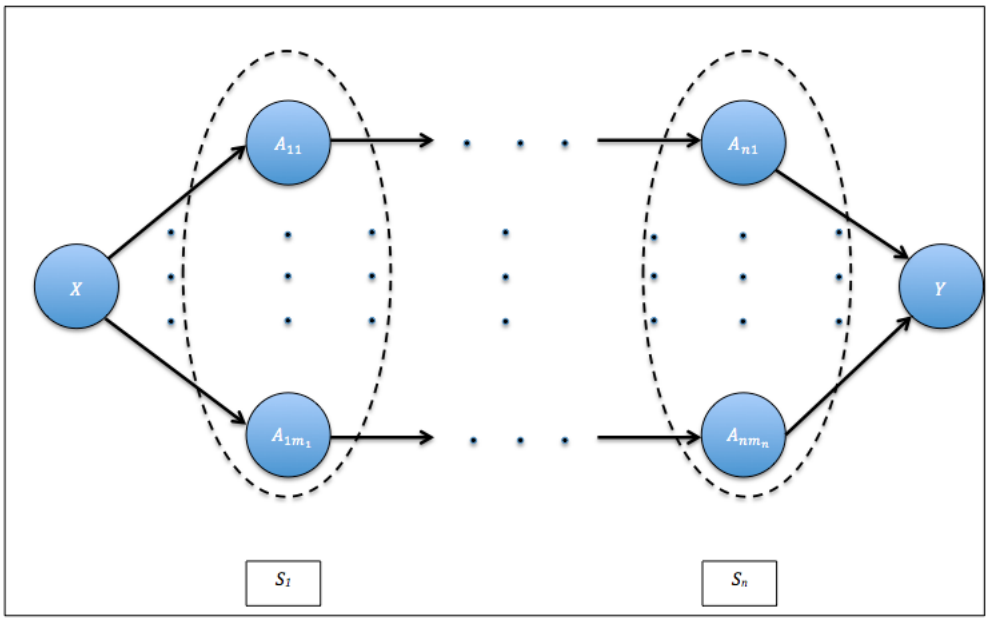

Fig. 5.1. Representation of a machine learning pipeline. This is represented as a generalized directed acyclic graph. S_i represents the i-th computational step in the pipeline and A_{ij} represents the j-th algorithm in the i-th step. X is the input dataset and Y is the evaluation metric.

Pipelines in machine learning and data science are commonly organized in the form of interdependent components. Such components that make up a data analytic pipeline include data preprocessing, feature extraction, feature transformation, model building and model evaluation among others. Such pipelines provide a natural way to organize such tasks, and they play a key part in the design and implementation of large scale data science projects. Machine learning toolboxes like scikit-learn [55], RapidMiner [56] and Apache Spark [57] independently provide frameworks for implementing pipelines. Fig. 5.1 shows a generic representation of data analytic pipelines. Each computational step of the pipeline S_i consists of several algorithms (A_{ij}) to choose from. Each algorithm in the pipeline consists of its own hyperparameters θ_{ijk} that must be optimized for using the algorithm. Therefore, there are an exponential number of combinations of algorithms and hyperparameters in a given analytic pipeline skeleton. This then is an extremely computationally intensive task of optimizing the pipeline. Tuning this pipeline can be viewed as the optimization of a blackbox objective function that is noisy and expensive to evaluate. The input to the blackbox are the input dataset X, the pipeline P(consisting of the steps S_i, the algorithms A_{ij}

and corresponding hyper-parameters θ_{ijk}) and the output performance Y such as validation error, accuracy, F1-score and cross-entropy loss among others, which are examples of the objective function.The goal of a data scientist is to find the best set of algorithms and hyper-parameters in this pipeline that optimizes the objective function. This corresponds to finding an optimal path through the pipeline in 5.1. Simple methods such as grid and random search [58] have been used to tackle this problem. More complicated approaches such as Bayesian optimization [59], [60] have been used successfully for approaching more difficult problems. Pipeline optimization as a whole has also been approached using genetic algorithms [61]–[63]. We use grid search, random search and bayesian optimization methods for optimization of the pipeline and each individual path in it.

Interpretation of machine learning pipelines is extremely important for their adoption in various domains. Domain experts do not prefer the use of black-box pipelines. They would prefer to understand how predictive decisions are made by the pipeline. Recently there has been an advent of models and techniques for improving the interpretability of machine learning. [64] introduces a model-agnostic method for interpreting machine learning blackboxes. [65] attempts at a definition of interpretability in this context and how it should be measured. [66] uses influence functions to understand blackbox predictions. In this work, we attempt to provide an interpretation of machine learning pipelines as a whole as opposed to the approaches which are geared toward interpretation of individual machine learning algorithms in general. This includes understanding the predictions with respect t other components like feature extraction and feature transformation and also to smaller components like individual hyper-parameters. To our knowledge, this type of approach to interpretation has not been done before. To this end, we propose the understanding of the contribution of error in data analytic pipelines. We use the cross-entropy loss as the performance metric of the optimization algorithms and basis of error quantification in the image classification pipelines. Understanding the source of the error in the predictive model is important for experts to design the data analytic pipelines. Experts can use the information from error contributions to focus attention on certain parts of the pipeline depending on the source of error. In addition, it also provides non-experts in machine learning insight into the predictions of the model. They can understand whether the error they are seeing are due to which component of the process. We introduce a methodology to quantify the contribution of error from different components of the data analytic pipeline, namely the computational

steps and algorithms in the pipeline.

Pipeline optimization algorithms like grid search, random search [58] and Bayesian optimization [59] are used to optimize the pipeline for performing experiments with the error quantification and propagation methodology. We take two different approaches to optimization. The first is hyper-parameter optimization (HPO) where a computational path in Fig. 5.1 is optimized. This is equivalent to a combined optimization of the hyperparameters of the algorithms on that path. The second type of optimization is denoted as combined algorithm selection and hyperparameter optimization (CASH). This is a more difficult problem, because the pipeline is optimized globally, in that the result of the optimization is a single optimized path that produces the best performance over all the paths in the machine learning workflow.

We use four datasets to demonstrate the error quantification and propagation methodology. The machine learning problem is that of image classification. We show the performance of both the optimization frameworks (HPO and CASH) for the experiments. We show experimentally that CASH using random search can be efficiently used for quantification of errors from the different computational steps of the pipeline. In addition, HPO frameworks of both Bayesian optimization and random search provides estimates of error contributions from the algorithms and hyperparameters in a particular path of the pipeline. We demonstrate from the results that the error quantification methodology maybe used by both data science and domain experts to improve and interpret the results of image classification pipelines.

The paper is organized as follows. Section 5.2 describes the methods that are used in this work and the proposed methodology of error contribution. The experimental frameworks, datasets, results and discussion makes up section 5.3. This is followed by the conclusion in section 5.4.

5.2 Foundations

In this section we describe the optimization problem and the black-box optimization methods that are used in this work.

5.2.1 Algorithm selection and hyper-parameter optimization

We approach the problem of optimization of the pipeline from two frameworks. In one framework, each path in the pipeline in 5.1 is individually optimized. This essentially boils down to problem of hyper-parameter optimization (HPO) because the hyperparameters of each algorithm are optimized for each individual path. In the second framework, the entire pipeline is optimized. This means that the algorithms and hyperparameters are optimized together. This is denoted as combined algorithm selection and hyper-parameter optimization (CASH).

5.2.1.1 Hyper-parameter optimization (HPO)

Let the n hyperparameters in a path be denoted as $\theta_1, \theta_2, ..., \theta_n$, and let $\Theta_1, \Theta_2, ..., \Theta_n$ be their respective domains. The hyperparameter space of the path is $\Theta = \Theta_1 \times \Theta_2 \times ... \times \Theta_n$.

When trained with $\theta \in \Theta$ on data D_{train}, the validation error is denoted as $\mathcal{L}(\theta, D_{train}, D_{valid})$. Using k-fold cross-validation, the hyperparameter optimization problem for a dataset D is to minimize:

$$f^D(\theta) = \frac{1}{k} \sum_{i=1}^{k} \mathcal{L}(\theta, D_{train}^{(i)}, D_{valid}^{(i)}) \tag{5.1}$$

Hyperparameters θ_i may be numerical, categorical or conditional with a finite domain. The minimization of this objective function provides the optimal configuration of hyperparameters on a particular path in the pipeline in Fig. 5.1.

5.2.1.2 Combined algorithm selection and hyper-parameter optimization (CASH)

We can define the CASH formulation using Fig. 1. Let there be n computational steps in the pipeline. Each step i in the pipeline consists of algorithms $A_i(\Theta_i)$, where $A_i(\Theta_i) = \{A_{i1}(\theta_{i1}), ..., A_{im_i}(\theta_{im_i})\}$, m_i is the number of algorithms in step i, A_{ij} represents the j-th algorithm in step i, and θ_{ij} represents the set of hyperparameters corresponding to A_{ij}. The entire space of algorithms and hyperparameters is therefore given by $\mathcal{A} = A_1(\Theta_1) \times A_2(\Theta_2) \times ... \times A_n(\Theta_n)$. The objective function to be minimized for CASH is given by

$$f^D(A) = \frac{1}{k} \sum_{i=1}^{k} \mathcal{L}(A, D_{train}^{(i)}, D_{valid}^{(i)}) \tag{5.2}$$

where, $A \in \mathcal{A}$ and other notations are the same as those introduced in the previous section.

5.2.2 Optimization methods

The critical step in HPO or CASH is to choose the set of trials in the search space, which is Θ for HPO and $\mathcal{A}$ for CASH. In this section, methods that are used in this paper for optimization of Eq. 5.1 and Eq. 5.2 are described. Grid search, random search and Bayesian optimization are used in this work.

5.2.2.1 Grid search

Grid search is the simplest of all methods for coming up with trials in the search space. The set of trials in grid search is formed by assembling every possible set of values in Θ and $\mathcal{A}$ and computing the validation loss for each. The configuration $\theta \in \Theta$ or $A \in \mathcal{A}$ that minimizes the validation loss $\mathcal{L}$ is chosen as the optimum configuration. Unfortunately grid search is computationally very expensive. For HPO, the number of trials corresponds to $\prod_{i=1}^{n} |\Theta_i|$, and for CASH this is $\prod_{i=1}^{n} |A_i(\Theta_i)|$. This product makes grid search suffer from the *curse of dimensionality*. This is because the number of trials grows exponentially with the number of hyperparameters. However, grid search has certain advantages. Firstly, parallelization and implementation is trivial. In addition, grid search is robust in the sense that results maybe replicated easily.

5.2.2.2 Random search

Random search is the optimization method where trial configurations are randomly sampled from the search space of HPO (Θ) or CASH ($\mathcal{A}$). [58] shows empirically and theoretically that randomly selecting trials is sufficiently accurate and more efficient than performing optimization using grid search. We also show similar results in this work.

5.2.2.3 Bayesian optimization

Sequential model based Bayesian optimization (SMBO) [67] is the method of choice when it comes to optimization of complicated black-box functions. In a nutshell, it consists of two components. The first is a probabilistic model and the second is an acquisition function. The probabilistic model can be modelled using Gaussian processes (Spearmint) [59], random forests (SMAC) [67] and using density estimation with Tree-structured Parzen estimators (TPE) [68]. The acquisition function determines the future candidates or trials

for evaluation. The acquisiton function is relatively cheap to evaluate compared to the actual objective function f^D. One of the most prominent acquisition functions is *expected improvement* (EI) [69]. We use the sequential model-based algorithm configuration (SMAC) that uses random forests as the Bayesian optimization framework. This is because it can be used for optimizing conditional hyperparameter configurations, and based on empirical results in [70].

5.3 Proposed methods

In this section the proposed methodology for quantification of error contribution is presented. The method is independent of the black-box optimization methods that maybe used for both the HPO and CASH formulations.

5.3.1 Error contribution with the agnostic methodology

Machine learning pipelines maybe understood and interpreted by quantifying the contribution of error from different parts of the pipeline. For example, it is useful for machine learning experts and domain experts to understand and identify where the source of the error is in a pipeline. Referring back to Fig. 5.1, if it was known that most of the error in the final result originated from feature extraction, then machine learning practitioners would devote more time and energy to coming up with better algorithms for feature extraction or fine-tuning the algorithms in that step to reduce the error. In addition, if it were possible to quantify the contribution of errors from certain algorithms or hyper-parameters in the pipeline, then the data scientists would try to fine tune the algorithms in the pipeline or even try to replace the algorithms with better alternatives.

We propose an *agnostic* methodology for quantifying error contributions from different parts of the pipeline. It is quantified as the minimum error obtained by being agnostic to a particular component of the pipeline (computational step or algorithms). We shall define what *agnostic* refers to for both computational steps and algorithms individually.

5.3.1.1 Quantification of error from computational steps

The *agnostic* methodology maybe used for quantification of error contributions from computational steps like feature extraction, data pre-processing and and learning algorithms. Being *agnostic* to a computational step means that the algorithms in that step are selected

randomly for that step while the remaining pipeline is optimized. The average of the minimum errors obtained with each algorithm in the step used as the only algorithm in that particular step, provides an estimate of the agnostic error from a particular pipeline. More formally, the agnostic methodology is implemented for computational steps in the following manner. Using 5.1 as a reference, let n be the number of steps in the pipeline. Each step in the pipeline is denoted as S_i. $|S_i|$ is the number of algorithms in step i. A_{ij} denotes the j-th algorithm in the i-th step. E^* represents the minimum validation error found after optimization of the entire pipeline (using the CASH framework). $E^*_{A_{ij}}$ is the minimum validation error found with A_{ij} as the only algorithm in step i. The error contribution from step i, $EC^*_{S_i}$ is given by Eq. 5.3.

$$EC^*_{S_i} = \frac{1}{|S_i|}\sum_{z=1}^{|S_i|} E^*_{A_{ij}} - E^*, \tag{5.3}$$

where, $i = 1, ..., n, j = 1, ..., |S_i|$ Taking the difference with respect to the global minimum in Eq. 5.3 provides an estimate of the error contribution from step i of the pipeline. A large value of $EC^*_{S_i}$ would mean that step S_i is important for the pipeline.

5.3.1.2 Quantification of error from algorithms

The *agnostic* methodology for algorithms is implemented as follows. Similar to the *agnostic* methodology for steps defined above, we define the *agnostic* methodology for algorithms. In this case, we focus on a single path in the pipeline in Fig. 1. Let's assume we are trying to quantify the error contribution of a particular algorithm A_{ij} that lies on path p. Being *agnostic* to A_{ij} means we optimize everything else on the path except the algorithm. This means that we pick the hyperparameters θ_{ij} of algorithm A_{ij} randomly while optimizing the rest of the algorithms on the path. This is formally calculated by taking the average of the optimum errors on the path for each configuration of θ_{ij}. The minimum validation error on the path is then subtracted from this error to give us the error contribution from algorithm A_{ij} on path p. These errors are computed using the results and the search trials on the CASH framework in section 5.2.1.2.

$$EC^*_{A_{ij}} = \frac{1}{|\theta_{ij}|}\sum_{z=1}^{|\theta_{ij}|} {E^z_{A_{ij}}}^* - E^*_{A^p_{ij}}, \tag{5.4}$$

where, $i = 1, ..., n, j = 1, ..., |\theta_{ij}|$, $|\theta_{ij}|$ represents the number of hyperparametric configurations of A_{ij}, ${E^z_{A_{ij}}}^*$ is the minimum error obtained with the z-th configuration of θ_{ij} and $E^*_{A^p_{ij}}$ is the minimum error found over the path p that consists of algorithm A_{ij}.

5.3.1.3 Quantification of error from hyper-parameters

The *agnostic* methodology for hyper-parameters is implemented as follows. In the case of hyper-parameters, we focus on a single path similar to what we did for algorithms. Let's assume we are trying to quantify the error contribution of a particular hyper-parameter θ_{ijk} that lies on path p, i.e. the k-th hyper-parameter of the j-th algorithm in the i-th step of the pipeline. Being *agnostic* to θ_{ijk} means we optimize everything else on the path except the hyper-parameter. This means that we pick the hyperparameter θ_{ijk} of algorithm A_{ij} randomly while optimizing the rest of the hyper-parameters on the path. This is formally calculated by taking the average of the optimum errors on the path for each configuration of θ_{ijk}. The minimum validation error on the path is then subtracted from this error to give us the error contribution from hyper-parameter θ_{ijk} on path p. This is again computed using the HPO framework described in section 5.2.1.1.

$$EC^*_{\theta_{ijk}} = \frac{1}{|\theta_{ijk}|} \sum_{z=1}^{|\theta_{ijk}|} {E^z_{\theta_{ijk}}}^* - E^*_{A^p_{ij}}, \tag{5.5}$$

where, $i = 1, ..., n, j = 1, ..., |\theta_{ij}|$, k = number of hyper-parameters of algorithm A_{ij}. $|\theta_{ijk}|$ represents the number of configurations of θ_{ijk}, ${E^z_{\theta_{ijk}}}^*$ is the minimum error obtained with the z-th configuration of θ_{ijk} and $E^*_{A^p_{ij}}$ is the minimum error found over the path p that consists of algorithm A_{ij}.

5.4 Experiments and results

In this section, we describe the experiments performed on the data analytic pipeline to quantify the error contributions and propagation from different components of the pipeline. Image classification is the data analytic problem chosen for demonstrating the error quantification experiments. A representation of an image classification pipeline is shown in Fig. 5.2 in the form of a flowchart.

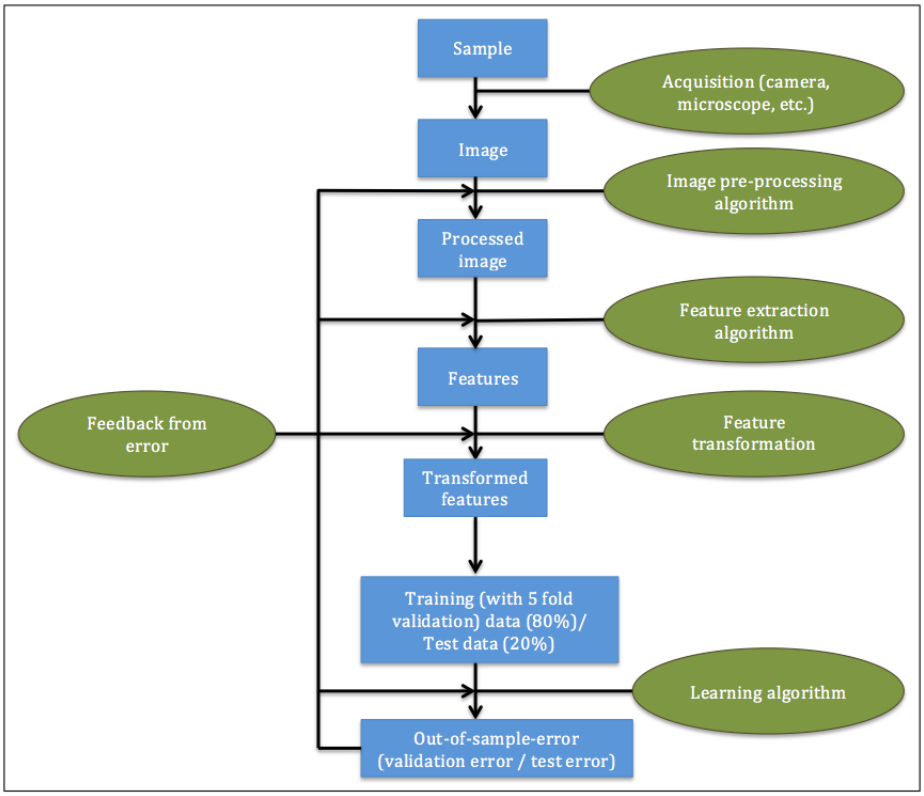

Fig. 5.2. Representation of an image classification pipeline. The pipeline consists of the steps represented by green ellipses and the outputs of each step represented by blue rectangles. In this work, we focus on the steps and outputs after pre-processing.

In this work, we focus on real world scientific datasets from the domains of medical pathology and material science. Therefore, the flowchart starts with a sample that is imaged with acquisition technology like a camera or a microscope. The image is then processed using image pre-processing algorithms like normalization and standardization. This may also include image segmentation algorithms. This is followed by feature extraction algorithms that extract useful information from the images. Sometimes, the features extracted are transformed to a different vector space using feature transformation (feature selection or dimensionality reduction) algorithms. The dataset is then divided into training and test datasets in a 80-20 split. Finally, classification algorithms like random forests [71] and support vector machines (SVM) [72] are used for learning in order to build a predictive model for the image classification problem. The performance of the pipeline is evaluated using classification metrics like F1-score, accuracy, precision and recall. We use the cross

entropy loss on the validation data as the estimate of the out-of-sample error. This error is then used as a feedback to quantify the contribution of the errors from different components of the pipeline. The specific pipeline used in this work is shown in the following figure.

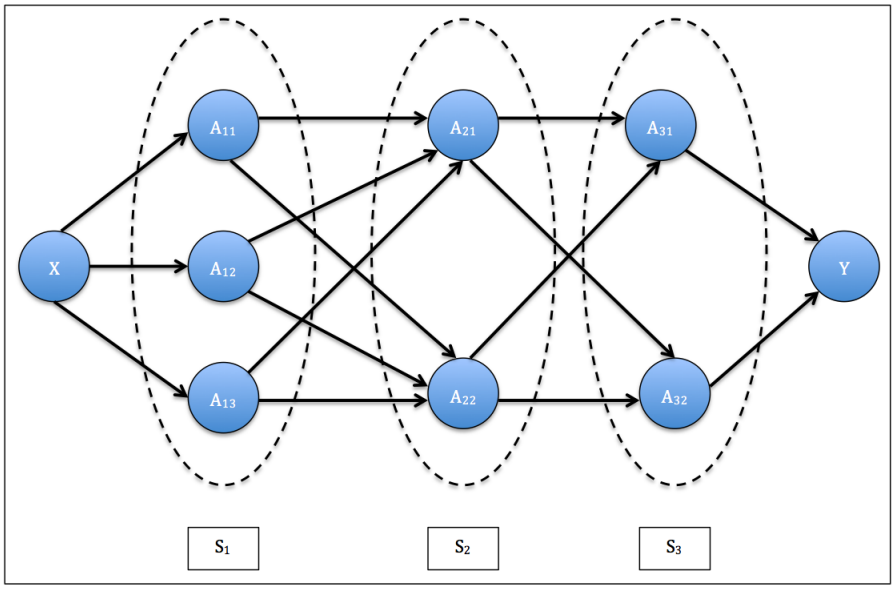

Fig. 5.3. Representation of the image classification pipeline as a directed acyclic graph used in this work. This is an instantiation of the generalized data analytic pipeline in Fig. 5.1

The above figure shows the pipeline used in this work. There are 3 computational steps in this pipeline, namely feature extraction (S_1), feature transformation (S_2) and learning algorithms (S_3). The steps, algorithms and corresponding hyperparameters $A_{ij}(\theta_{ij})$ is described in Table 5.1.

Table 5.1. Algorithms and hyper-parameters used in the image classification pipeline. The specific algorithms and corresponding *hyperparameters* are defined in the last column

Step	$A_{ij}(\theta_{ij})$	Definition
Feature extraction	$A_{11}(\theta_{11})$	Haralick texture features (*distance*)
	$A_{12}(\theta_{12})$	Pre-trained CNN trained on ImageNet [1] database with VGG16 [73] network
	$A_{13}(\theta_{13})$	Pre-trained CNN trained on ImageNet [1] database with Inception [74] network
Feature transformation	$A_{21}(\theta_{21})$	PCA (*whitening*) [53]
	$A_{22}(\theta_{22})$	ISOMAP (*number of neighbors, number of components*) [75]
Learning algorithms	$A_{31}(\theta_{31})$	Random forests (*number of trees, maximum features*) [71]
	$A_{32}(\theta_{32})$	SVM (C, γ) [72]

The algorithms defined above in the table are selected for making up the components of the pipeline in Fig. 5.3. This is meant to serve as an example for demonstrating the experiments using the error contribution framework described in section 5.3. It can easily be generalized to any data analytic problem that involve pipelines.

5.4.1 Optimization frameworks

Experiments are performed using two optimization frameworks. These frameworks have been described in detail in Section 5.2.1. The first global optimization framework is the CASH framework described in Section 5.2.1.2. Here, the pipeline is optimized as a whole including the algorithms, which are themselves considered as hyper-parameters in this framework. The following figure is a representation of this. This is used for quantification of the contribution of error with respect to *computational steps* in the pipeline.

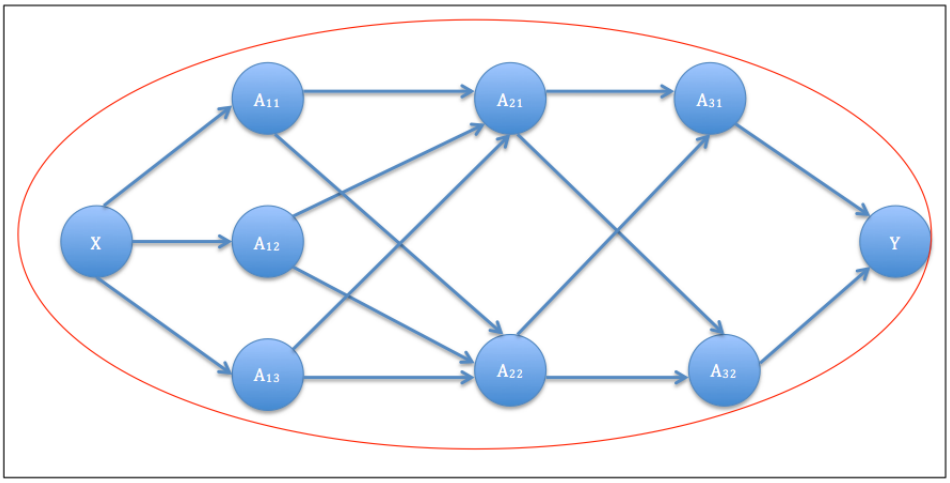

Fig. 5.4. Combined algorithm selection and hyper-parameter optimization in a data analytic pipeline. The algorithms and corresponding hyper-parameters are optimized simultaneously.

The second framework is the hyperparameter optimization (HPO) framework where each path in the pipeline is optimized individually. This is described in detail in section 5.2.1.1. This framework is used for quantifying the contribution and propagation of error with respect to *algorithms* in the each path of the pipeline.

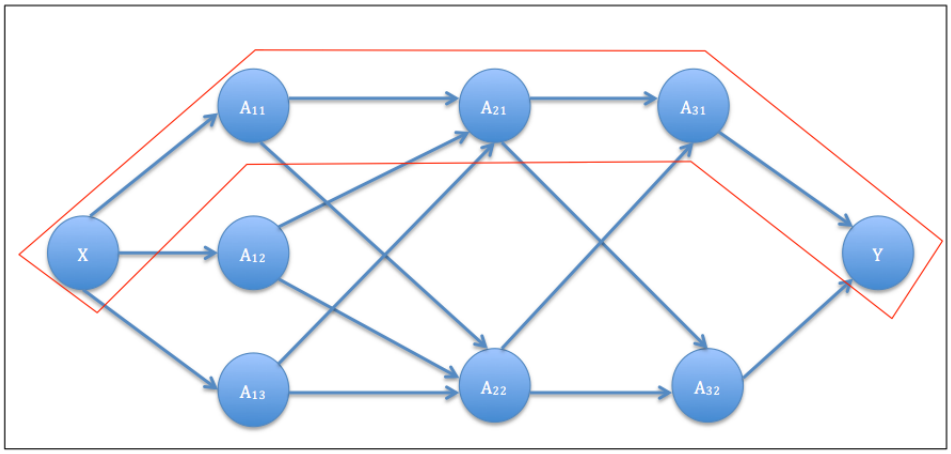

Fig. 5.5. Hyper-parameter optimization in a data analytic pipeline. Each path in the pipeline is individually optimized.

Specifically, we choose the path *haralick texture features* - *PCA* - *random forests* to demonstrate the error quantification approach for algorithms.

5.4.2 Datasets

Four datasets from the domains of medicine and material science are used in this work. They are image datasets of breast cancer [76], brain cancer [77], and two datasets of microstructures in material science [78]. They are described in the following table.

Table 5.2. Notations for error definitions used in the error propagation model

Dataset (notation)	Distribution of classes
Breast cancer (*breast*) [76]	*benign*: 151, *in-situ*: 93, *invasive*: 202
Brain cancer (*brain*) [77]	*glioma*: 16, *healthy*: 210, *inflammation*: 107
Material science 1 (*matsc1*) [78]	*dendrites*: 441, *non-dendrites*: 132
Material science 2 (*matsc2*) [78]	*transverse*: 393, *longitudinal*: 48

The above table represents datasets from the scientific domain. These datasets have been chosen because they represent examples of real world datasets. They are noisy in the sense that they have artefacts in the images, are heavily imbalanced and are small in terms of number of samples. They are different from the very large datasets like ImageNet [1], where deep learning techniques like convolutional neural networks have been shown to be superior. Even though deep neural networks represent an end-to-end workflow where the input image is fed into the network and the output classification is obtained at the other end, they may also be represented as pipelines, if the hyper-parameters of the network are considered. [79] has shown that machine learning problems involving datasets from medical imaging may be solved using pre-trained and fine-tuned neural networks rather than training them from scratch. We have therefore used pre-trained models such as VGGnet [73] and InceptionNet [74] as pre-trained feature extraction models that fit naturally in the pipeline framework described here for the purpose of illustrating the error quantification methodology.

5.4.3 Error quantification experiments

Experiments based on the quantification of error contributions framework described in section 5.3.1 are presented here. The plots are of the error contribution values calculated using Eqs. 5.3, 5.4 and 5.8 on the 4 datasets described in Table 5.2.

5.4.3.1 Experimental setting

Optimization using the 3 algorithms in section 5.2.2 is performed using the pipeline in Fig. 5.3 on the 4 datasets in Table 5.2. The domain and possible values of the hyper-

parameters are described in the following table. The convergence criteria (a hyper-hyper-parameter) is set at 50 iterations of unchanging function value for each of the optimization methods. The choice of the convergence criteria and hyper-parameters are independent of the error quantification methods. Results maybe obtained by using any choice of values for these components. The continuous hyper-parameters *maximum features*, C and γ have been described specifically for comparison of the optimization methods with grid search. In general, discretization of the hyper-parameters is not necessary for performing optimization. The error contribution values are obtained from the trials in the optimization methods

Table 5.3. Hyper-parameter domains corresponding the algorithms in Table 5.1 used by the optimization methods

Hyper-parameter	Values
distance	[1, 2, 3, 4]
whitening	[True, False]
number of neighbors	[3, 4, 5, 6, 7]
number of components	[2, 3, 4]
number of estimators	[8, 81, 154, 227, 300]
maximum features	[0.3, 0.5, 0.7]
C	[0.1, 25.075, 50.05, 75.025, 100.0]
γ	[0.3, 0.5, 0.7]

described in Section 5.2. Grid search is only run once while the other algorithms are averaged over 5 runs with the mean and standard deviation shown in the following plots. These results are computed on the validation error (cross-entropy loss) obtained at the end of the pipeline. Random search and Bayesian optimization (using the SMAC algorithm) are implemented on both the frameworks described in Section 5.4.1. The grid search results maybe used as the gold standard to compare the performance of other optimization algorithms.

5.4.3.2 Error contribution from computational steps

The mean and standard deviation values of EC_{S_i} calculated using Eq. 5.3 is represented in Fig. 5.6 for the 4 datasets in Table 5.2. The error is calculated using the formulation of EC_{S_i} in section 5.3.1.1. We observe that most of the contribution comes from feature extraction algorithms. This means that it is most important to optimize the feature extraction step among the other steps as it is of most importance based on the plots. This confirms our intuitive belief that feature extraction algorithms are the most important components of a machine learning pipeline.

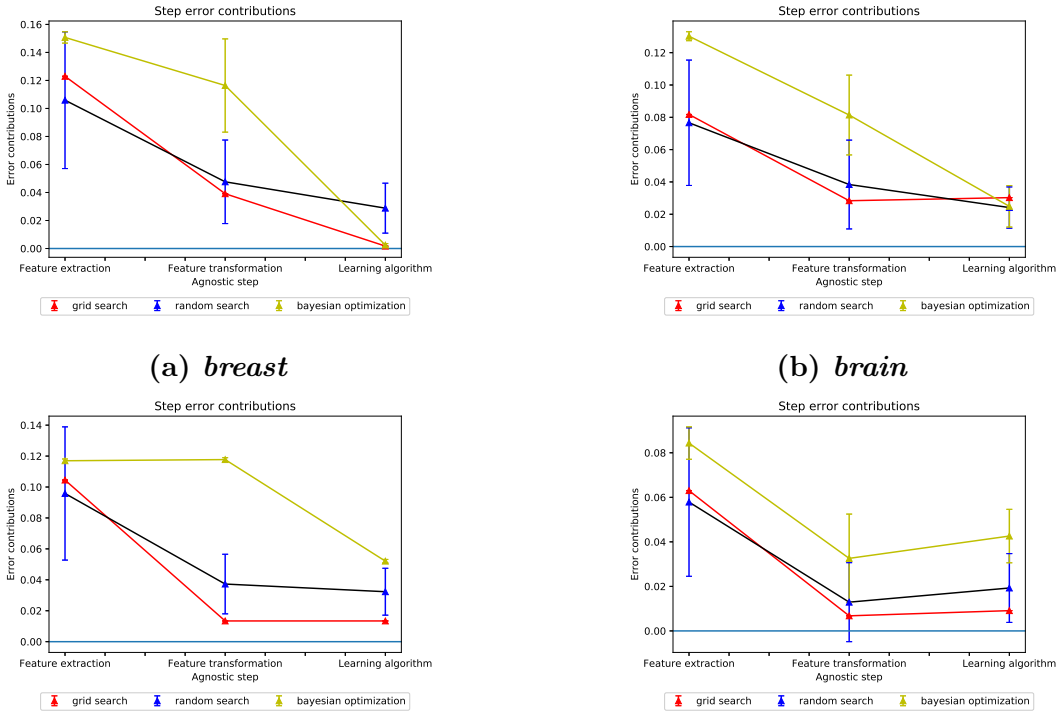

(a) ***breast*** (b) ***brain***

(c) ***matsc1*** (d) ***matsc2***

Fig. 5.6. Plots of error contributions from computational steps in the pipeline. Random search (blue) follows the behavior of grid search (red) more accurately than Bayesian optimization (yellow). Hence, random search maybe used to quantify the error contributions instead of grid search.

The standard deviation of grid search is 0 because it was only run once for each dataset due to the time required for computation and also because of the robustness of the grid search method (the results don't change because we try out every single configuration). We observe from the results, that random search follows the behavior of grid search. It mirrors the behavior of grid search, but the results are not robust because of the high standard deviation. This is expected because the search trials may not include all the configurations in the pipeline as opposed to grid search where all the configurations of algorithms and hyperparameters are evaluated. The results of SMAC (bayesian optimization) in the CASH framework do not follow the behavior of grid search as closely as random search. This is because the trials for SMAC are even more sparse with respect to the algorithms it selects for optimization of the error in Eq. 5.3. SMAC only samples a few configurations based on the updated probabilistic model as it narrows in on the optimum configuration. Therefore, it sometimes gives erroneous results as can be seen by the contribution of feature transformation

in Fig. 5.6.

5.4.3.3 Error contribution from algorithms

In the following figure, the error contributions from algorithms are quantified using the formulation in Section 5.3.1.2. We select *haralick texture features*, *PCA* and *random forests* as the path to demonstrate the contribution of error from algorithms, because each of these algorithms are associated with one or more hyper-parameters. We observe a trend here, in that, the contribution from *haralick texture features* and *random forests* is more than *PCA*. This means that it is more important to tune *haralick texture features*, and *random forests* than it is to tune *PCA*. This maybe attributed to the fact that the search space of hyperparameters (in Table 5.3) for *haralick texture features* and *random forests* is larger than that of *PCA*. Again, we see the trend that random search performs better and is more robust in terms of following the behavior of grid search than Bayesian optimization.

5.4.3.4 Error contribution from hyper-parameters

Fig. 5.8 shows the error contributions from hyper-parameters quantified using the formulation in Section 5.3.1.3. We again select *haralick texture features*, *PCA* and *random forests* as the path to demonstrate the contribution of error from algorithms. The hyper-parameters (from Table 5.3) in this path are *Haralick distance*, *whitening*, *Number of etimators* and *Maximum features*. Again, we see the trend that random search performs better in terms of following the behavior of grid search than Bayesian optimization. In addition, we observe that it is in general more important to tune the hyper-parameters *Haralick distance*, and *Number of estimators* than it is to tune the other hyper-parameters. This is again could be due to the number of configurations of the respective hyper-parameters in Table 5.3, where a hyper-parameter with a larger search space has more contribution to the error and is therefore more important to tune.

5.4.3.5 Comparison of computation time

Fig. 5.9 shows the average computation times of each of the algorithms used in the error quantification experiments. We can observe that random search and bayesian optimization are both efficient in terms of computational time as opposed to grid search. Therefore, both CASH and HPO optimization frameworks using algorithms like Random search and Bayesian

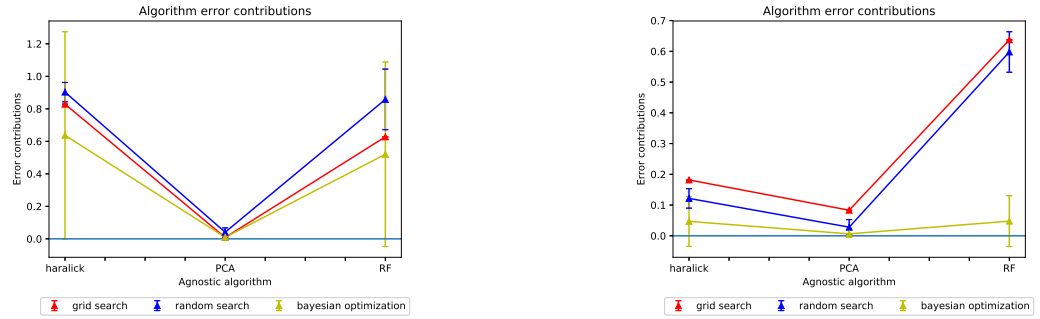

(a) ***breast***

(b) ***brain***

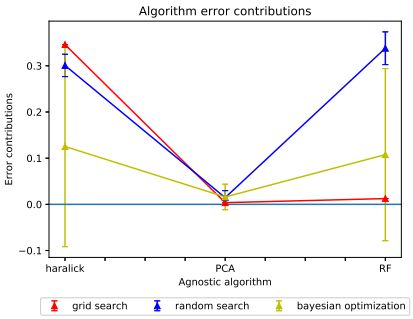

(c) ***matsc1***

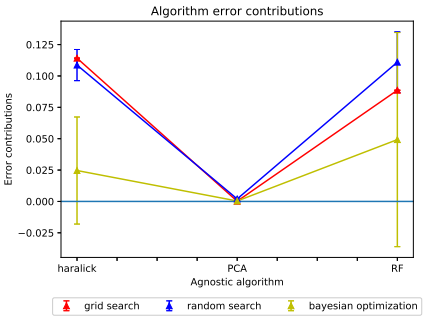

(d) ***matsc2***

Fig. 5.7. Plots of error contributions from algorithms in the pipeline. Random search again mirrors the trend of grid search more than bayesian optimization. Therefore random search maybe used instead of grid search for computing the contribution of error from algorithms in a path. The plots also show that it is more important to tune *haralick texture features*, and *random forests* than it is to tune PCA.

optimization maybe used for computation of the error contributions instead of grid search. However, as we have seen repeatedly from the plots in Figs. 5.6, 5.7 and 5.8; random search captures the behavior of grid search more accurately and is more robust than grid-search. Hence, random search maybe used to quantify the contributions from steps, algorithms and hyper-parameters accurately and efficiently.

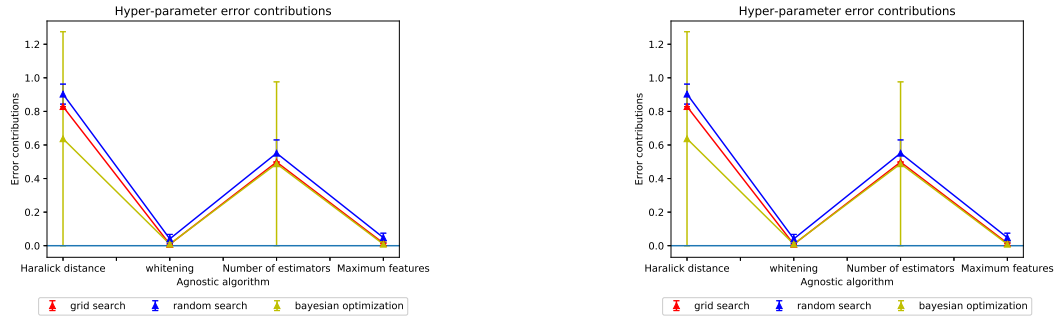

(a) *breast* (b) *brain*

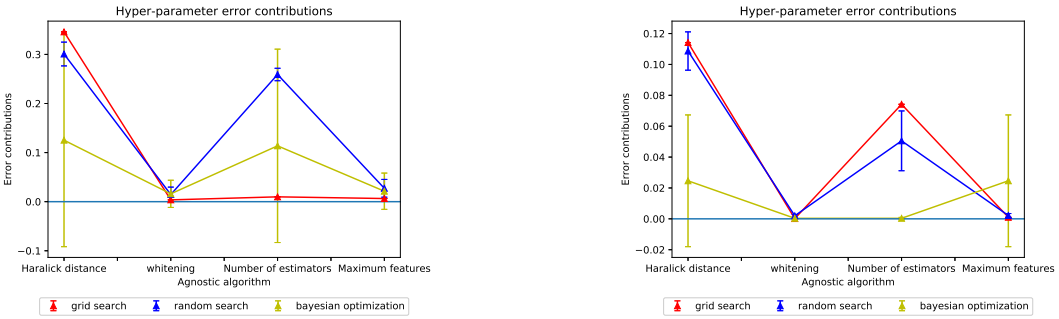

(c) *matsc1* (d) *matsc2*

Fig. 5.8. Plots of error contributions from hyper-parameters in the pipeline. Random search again mirrors the trend of grid search more than bayesian optimization. Therefore random search maybe used instead of grid search for computing the contribution of error from hyper-parameters in a path. The plots also show that it is more important to tune the hyper-parameters *Haralick distance*, and *Number of estimators* than it is to tune the other hyper-parameters.

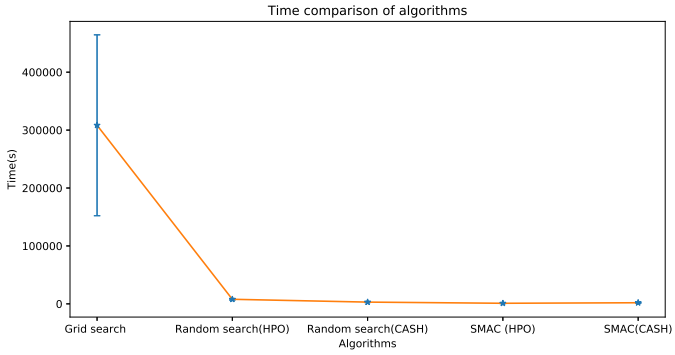

Fig. 5.9. Comparison of computational time for running each of the 3 optimization methods in the two optimization frameworks (HPO and CASH) in section 5.2.1 averaged over the 4 datasets in Table 5.2. Random search and bayesian optimization are both much more efficient that grid search in terms of computation time and maybe used to quantify the error contribution more efficiently than grid search.

5.5 Conclusion

This work proposes a methodology for making black box machine learning based image classification pipelines interpretable. The suggested approach involves understanding the sources of error contribution in data analytic pipelines. Specifically, we propose a methodology to quantify the error contributions from different parts of an image classification pipeline, namely computational steps, algorithms and hyper-parameters. This methodology is described as the *agnostic* method in Section 5.3.1. The results in Section 5.4.3 show that the black-box optimization methods like random search and Bayesian optimization is able to quantify the error contributions as well as grid search. The framework of Bayesian optimization is not as accurate and robust as random search due to reasons specified in section 5.4. In general we expect optimization algorithms that have more trials in a larger region of the search space of the configurations to quantify the contributions from components in the pipeline accurately. We intend to explore the results from more hyper-parameter optimization algorithms in the future. The error quantification methodology maybe used by machine learning practitioners to understand and interpret results of a specific machine learning problem on a dataset. Understanding the source of error in terms of steps, algorithms and hyper-parameters will help data scientists quickly iterate over pipelines, algorithms and hyperparameters and find the best set of configurations for solving a particular task by focussing on the important components of the pipeline found from the results of error contribution. In addition domain experts like biologists and scientists from different disciplies can use this method to understand and interpret where the error is coming from in the pipeline they use to solve their specific image classification problem. In terms of future work, this formulation could be expanded to cover more data analytic problems that involve complicated algorithms. For example, this framework maybe used to interpret problems in other applications like speech recognition, text classification and even unsupervised machine learning problems. Essentially, the error quantification framework maybe used by any practitioner that works with pipelines for solving a machine learning problem. The pipeline may even be extended to include processes like data cleaning. This framework may also be included to understand and interpret deep neural networks, which are end-to-end in nature. This maybe used for comparing the performance of candidate networks for solving the problem.

CHAPTER 6
CONCLUSIONS AND FUTURE WORK

6.1 Conclusions

We investigate methods and algorithms to perform optimization and quantification of error in image classification pipelines. Our work revolves around the fact that the error observed as the classification metrics at the end of image classification pipelines is due to the accumulation and propagation of error from different components of the the image classification pipeline. To this end, we present the work done on four different projects. Two of the projects are focused on minimization of error with respect to different perspectives in the image classification pipeline. The first involves the minimization of error from the data analytic steps in the pipeline as a whole using exhaustive grid search. This method finds the best configuration of algorithms and hyper-parameters that minimize the cross-validation error for two classification tasks in the domain of material science. We also show that pre-trained convolutional neural networks maybe used to as a good feature representation for dendritic and non-dendritic microstructures. The second project proposes a method to generate artificial data using a parametric 3D model of blood vessels. This is used as a data augmentation procedure to reduce the error in image classification caused due to class imbalance. Class imbalance is a common source of error in image classification problems in the medical domain. We show empirical results that this method of generating artificial 3D models of vasculature can characterize the morphology of blood vessels in neuropathological tissue samples. In the second part of the thesis, we tackle the problem of quantification of error from different parts of an image classification pipeline. A lot of work has been done in the minimization of error in image classification with respect to optimizing different components in the pipeline. However, little attention has been paid to understanding the origin of error from the components of the workflow. The first project in this part involves the quantification of the quality of an image using a machine learning based score. This score can automatically suggest to a domain expert whether an image should or should not be used for further analysis. This provides a way to filter the image datasets in scientific domains based on the quality of images for analysis. The second project proposes a methodology to quantify the contribution of error in image classification pipelines using an *agnostic* methodology.

This method is able to quantify the contribution of errors from computational steps and algorithms in the pipeline. This provides a way for domain experts and data scientists to diagnose and profile an image classification pipeline and improve them based on the results. In addition, we also show that hyperparameter optimization techniques like random search can compute the contribution of errors similar to exhaustive grid search.

6.2 Future work

There are various extensions that could be made in terms of future work.

1. The exhaustive grid search approach for characterizing microstructures in the domain of material science can be used as a standard technique for finding the best configuration of algorithms and hyper-parameters for an image classification problem in that domain. In addition, more research can be performed to improve upon the pre-trained convolutional neural networks that have been successfully used to characterize images of microstructures in material science.

2. The problem of data or class imbalance is rampant in the scientific domain and in particular in the medical domain. Therefore, the parametric 3D model approach to perform data augmentation can be used as a data balancing methodology in other scientific domains that involve the analysis of images.

3. The *Quality of Image* score described in the first project maybe improved by using more sophisticated techniques and algorithms to quantify the error. In addition, the method can also be used to test the efficacy of the approach if more data from the same dataset is available. The experiment would take the form of comparing the results of data analysis using the entirety of the unfiltered dataset and the filtered *good* dataset using the score. The hypothesis then is that the results from the *good* dataset is better because it consists of images that consist of high quality image samples.

4. The *agnostic* methodology to quantify the error contribution in image classification pipelines in scientific domains can also be extended to include to understand and interpret end-to-end models like convolutional neural networks. In that case, the error contributions could be computed with respect to the layers of the neural network and could help deep learning experts to diagnose the source of error in the models. In

addition, this work may also be extended to other data domains and pipelines like machine learning workflows based on text and speech in natural language processing. This approach maybe used to quantify errors in any pipeline system that involves an optimization framework.

REFERENCES

[1] J. Deng, W. Dong, R. Socher, L.-J. Li, K. Li, and L. Fei-Fei, "Imagenet: A large-scale hierarchical image database," in *Computer Vision and Pattern Recognition, 2009. CVPR 2009. IEEE Conference on*, 2009, pp. 248–255.

[2] H. Xu, R. Liu, A. Choudhary, and W. Chen, "A machine learning-based design representation method for designing heterogeneous microstructures," *Journal of Mechanical Design*, vol. 137, no. 5, p. 051403, 2015.

[3] J. R. Rodgers and D. Cebon, "Materials informatics," *MRS Bulletin*, vol. 31, pp. 975–980, 12 2006, [Online]. Available: http://journals.cambridge.org/article_S0883769400011702

[4] S. Broderick, C. Suh, J. Nowers, B. Vogel, S. Mallapragada, B. Narasimhan *et al.*, "Informatics for combinatorial materials science," *JOM*, vol. 60, no. 3, pp. 56–59, 2008, [Online]. Available: http://dx.doi.org/10.1007/s11837-008-0035-x

[5] K. F. Ferris, L. M. Peurrung, and J. M. Marder, "Materials informatics: Fast track to new materials," *Advanced Materials & Processes, 165 (1): 50-51*, vol. 165, no. PNNL-SA-52427, 2007.

[6] S. R. Kalidindi, S. R. Niezgoda, and A. A. Salem, "Microstructure informatics using higher-order statistics and efficient data-mining protocols," *JOM*, vol. 63, no. 4, pp. 34–41, 2011, [Online]. Available: http://dx.doi.org/10.1007/s11837-011-0057-7

[7] B. G. S. Sergei V. Kalinin and R. K. Archibald, "Big-deep-smart data in imaging for guiding materials design," *Nature Materials*, vol. 14, pp. 973–980, September 2015.

[8] B. L. DeCost and E. A. Holm, "A computer vision approach for automated analysis and classification of microstructural image data," *Computational Materials Science*, vol. 110, pp. 126 – 133, 2015, [Online]. Available: http://www.sciencedirect.com/science/article/pii/S0927025615005066

[9] R. J. Schaefer and D. J. Lewis, "Directional solidification in a agcusn eutectic alloy," *Metallurgical and Materials Transactions A: Physical Metallurgy and Materials Science*, vol. 36A, pp. 2775–2783, October 2005.

[10] J. Mao and D. J. Lewis, *Nucleation promotion of Sn-Ag-Cu lead-free solder alloys via micro alloying.*, 2014, [Online]. Available: http://libproxy.rpi.edu/login?url=http://search.ebscohost.com/login.aspx?direct=true&db=cat02306a&AN=rlc.3566213&site=eds-live&scope=site

[11] T. C. Z.H. Barber, J.A. Leake, "The doitpoms project - a web-based initiative for teaching and learning materials science," *J. Mater. Educ.*, vol. 29, no. 1-2, pp. 7–16, 2003.

[12] E. Keogh and A. Mueen, "Encyclopedia of machine learning." Boston, MA: Springer US, 2010, ch. Curse of Dimensionality, pp. 257–258, [Online]. Available: http://dx.doi.org/10.1007/978-0-387-30164-8_192

[13] R. M. Haralick, K. Shanmugam, and I. H. Dinstein, "Textural features for image classification," *Systems, Man and Cybernetics, IEEE Transactions on*, no. 6, pp. 610–621, 1973.

[14] N. Dalal and B. Triggs, "Histograms of oriented gradients for human detection," in *Computer Vision and Pattern Recognition, 2005. CVPR 2005. IEEE Computer Society Conference on*, 2005, vol. 1, pp. 886–893.

[15] T. Ojala, M. Pietikäinen, and T. Mäenpää, "Multiresolution gray-scale and rotation invariant texture classification with local binary patterns," *IEEE Transactions on Pattern Analysis and Machine Intelligence*, vol. 24, no. 7, pp. 971–987, 2002.

[16] M.-K. Hu, "Visual pattern recognition by moment invariants," *IRE Transactions on Information Theory*, vol. 8, no. 2, pp. 179–187, 1962.

[17] N. Otsu, "A threshold selection method from gray-level histograms," *Automatica*, vol. 11, no. 285-296, pp. 23–27, 1975.

[18] A. Khotanzad and Y. H. Hong, "Invariant image recognition by zernike moments," *IEEE Transactions on Pattern Analysis and Machine Intelligence*, vol. 12, no. 5, pp. 489–497, 1990.

[19] W. Lievers and A. Pilkey, "An evaluation of global thresholding techniques for the automatic image segmentation of automotive aluminum sheet alloys," *Materials Science and Engineering: A*, vol. 381, no. 1?2, pp. 134 – 142, 2004, [Online]. Available: http://www.sciencedirect.com/science/article/pii/S0921509304003703

[20] J. Yang, Y.-G. Jiang, A. G. Hauptmann, and C.-W. Ngo, "Evaluating bag-of-visual-words representations in scene classification," in *Proceedings of the international workshop on multimedia information retrieval*, 2007, pp. 197–206.

[21] H. Bay, T. Tuytelaars, and L. Van Gool, "Surf: Speeded up robust features," in *Computer vision–ECCV 2006*. Springer, 2006, pp. 404–417.

[22] Y. Jia, E. Shelhamer, J. Donahue, S. Karayev, J. Long, R. Girshick *et al.*, "Caffe: Convolutional architecture for fast feature embedding," *arXiv preprint arXiv:1408.5093*, 2014.

[23] A. Krizhevsky, I. Sutskever, and G. E. Hinton, "Imagenet classification with deep convolutional neural networks," in *Advances in Neural Information Processing Systems 25*, F. Pereira, C. J. C. Burges, L. Bottou, and K. Q. Weinberger, Eds. Curran Associates, Inc., 2012, pp. 1097–1105, [Online]. Available: http://papers.nips.cc/paper/4824-imagenet-classification-with-deep-convolutional-neural-networks.pdf

[24] K. Klinger, Ed., *Machine Learning: Concepts, Methodologies, Tools and Applications*. IGI Global, 2012, vol. 1.

[25] P. Indyk and R. Motwani, "Approximate nearest neighbors: towards removing the curse of dimensionality," in *Proceedings of the thirtieth annual ACM symposium on Theory of computing*, 1998, pp. 604–613.

[26] G. H. Dunteman, *Principal Components Analysis*. Sage Publications, Inc., 1989, vol. 69.

[27] R. G. Lomax and D. L. Hahs-Vaughn, *Statistical concepts: A second course*. Routledge, 2013.

[28] H. Liu and R. Setiono, "Chi2: Feature selection and discretization of numeric attributes," in *In Proceedings of the Seventh International Conference on Tools with Artificial Intelligence*, 1995, pp. 388–391.

[29] R. Kohavi and G. H. John, "Wrappers for feature subset selection," *Artificial intelligence*, vol. 97, no. 1, pp. 273–324, 1997.

[30] M. A. Hall, "Correlation-based feature selection for machine learning," Ph.D. dissertation, The University of Waikato, 1999.

[31] M. A. Hearst, S. T. Dumais, E. Osman, J. Platt, and B. Scholkopf, "Support vector machines," *Intelligent Systems and their Applications, IEEE*, vol. 13, no. 4, pp. 18–28, 1998.

[32] L. Breiman, "Random forests," *Machine learning*, vol. 45, no. 1, pp. 5–32, 2001.

[33] T. Denoeux, "A k-nearest neighbor classification rule based on dempster-shafer theory," *IEEE Transactions on Systems, Man and Cybernetics*, vol. 25, no. 5, pp. 804–813, 1995.

[34] R. E. Schapire, Y. Freund, P. Bartlett, and W. S. Lee, "Boosting the margin: A new explanation for the effectiveness of voting methods," *Annals of statistics*, pp. 1651–1686, 1998.

[35] I. Rish, "An empirical study of the naive bayes classifier," in *IJCAI 2001 workshop on empirical methods in artificial intelligence*, 2001, vol. 3, no. 22, pp. 41–46.

[36] S. B. Kotsiantis, I. Zaharakis, and P. Pintelas, "Supervised machine learning: A review of classification techniques," 2007.

[37] P. C. Pattan, V. Mytri, and P. Hiremath, "Classification of cast iron based on graphite grain morphology using neural network approach," in *Second International Conference on Digital Image Processing*, 2010, vol. 7546, p. 75462S.

[38] P. Prakash, V. Mytri, and P. Hiremath, "Comparative analysis of spectral and spatial features for classification of graphite grains in cast iron," *Sci. Technol*, vol. 29, pp. 31–40, 2011.

[39] A. Kumara, V. Sundararaghavan, M. DeGraefb, and L. Nguyenb, "A markov random field approach for microstructure synthesis," *Modelling Simul. Mater. Sci. Eng.*, vol. 24, no. 035015, pp. 1–13, 2016.

[40] J. MacSleyne, J. Simmons, and M. D. Graef, "On the use of 2-d moment invariants for the automated classification of particle shapes," *Acta Materialia*, vol. 56, no. 3, pp. 427 – 437, 2008, [Online]. Available: http://www.sciencedirect.com/science/article/pii/S1359645407006702

[41] J. V. Sluytman and T. Pollock, "Optimal precipitate shapes in nickel-base ???? alloys," *Acta Materialia*, vol. 60, no. 4, pp. 1771 – 1783, 2012, [Online]. Available: http://www.sciencedirect.com/science/article/pii/S1359645411008706

[42] G. Impoco and L. Tuminello, "Incremental learning to segment micrographs," *Computer Vision and Image Understanding*, vol. 140, pp. 144 – 152, 2015, [Online]. Available: http://www.sciencedirect.com/science/article/pii/S1077314215000533

[43] R. Bostanabad, A. T. Bui, W. Xie, D. W. Apley, and W. Chen, "Stochastic microstructure characterization and reconstruction via supervised learning," *Acta Materialia*, vol. 103, pp. 89 – 102, 2016, [Online]. Available: http://www.sciencedirect.com/science/article/pii/S1359645415007259

[44] W. Z. Taffese, E. Sistonen, and J. Puttonen, "Caprm: Carbonation prediction model for reinforced concrete using machine learning methods," *Construction and Building Materials*, vol. 100, pp. 70 – 82, 2015, [Online]. Available: http://www.sciencedirect.com/science/article/pii/S0950061815304165

[45] Y. Guo, Y. Liu, A. Oerlemans, S. Lao, S. Wu, and M. S. Lew, "Deep learning for visual understanding: A review," *Neurocomputing*, vol. 187, pp. 27 – 48, 2016, [Online]. Available: http://www.sciencedirect.com/science/article/pii/S0925231215017634

[46] J. Yang, Y.-G. Jiang, A. G. Hauptmann, and C.-W. Ngo, "Evaluating bag-of-visual-words representations in scene classification," in *Proceedings of the international workshop on Workshop on multimedia information retrieval*, 2007, pp. 197–206.

[47] T. Heimann and H.-P. Meinzer, "Statistical shape models for 3d medical image segmentation: a review," *Medical image analysis*, vol. 13, no. 4, pp. 543–563, 2009.

[48] A. Krizhevsky, I. Sutskever, and G. E. Hinton, "Imagenet classification with deep convolutional neural networks," in *Advances in neural information processing systems*, 2012, pp. 1097–1105.

[49] M. J. Gerdes, C. J. Sevinsky, A. Sood, S. Adak, M. O. Bello, A. Bordwell *et al.*, "Highly multiplexed single-cell analysis of formalin-fixed, paraffin-embedded cancer tissue," *Proceedings of the National Academy of Sciences*, vol. 110, no. 29, pp. 11 982–11 987, 2013.

[50] R. M. Haralick, "Statistical and structural approaches to texture," *Proceedings of the IEEE*, vol. 67, no. 5, pp. 786–804, 1979.

[51] R. M. Haralick, K. Shanmugam *et al.*, "Textural features for image classification," *IEEE Transactions on systems, man, and cybernetics*, no. 6, pp. 610–621, 1973.

[52] N. V. Chawla, K. W. Bowyer, L. O. Hall, and W. P. Kegelmeyer, "Smote: synthetic minority over-sampling technique," *Journal of artificial intelligence research*, vol. 16, pp. 321–357, 2002.

[53] S. Wold, K. Esbensen, and P. Geladi, "Principal component analysis," *Chemometrics and intelligent laboratory systems*, vol. 2, no. 1-3, pp. 37–52, 1987.

[54] L. D. Harrison, "The validity of self-reported data on drug use," *Journal of Drug Issues*, vol. 25, no. 1, pp. 91–111, 1995.

[55] F. Pedregosa, G. Varoquaux, A. Gramfort, V. Michel, B. Thirion, O. Grisel *et al.*, "Scikit-learn: Machine learning in python," *Journal of machine learning research*, vol. 12, no. Oct, pp. 2825–2830, 2011.

[56] I. Mierswa, M. Wurst, R. Klinkenberg, M. Scholz, and T. Euler, "Yale: Rapid prototyping for complex data mining tasks," in *Proceedings of the 12th ACM SIGKDD international conference on Knowledge discovery and data mining*, 2006, pp. 935–940.

[57] A. Spark, "Apache spark: Lightning-fast cluster computing," *URL http://spark. apache. org*, 2016.

[58] J. Bergstra and Y. Bengio, "Random search for hyper-parameter optimization," *Journal of Machine Learning Research*, vol. 13, no. Feb, pp. 281–305, 2012.

[59] J. Snoek, H. Larochelle, and R. P. Adams, "Practical bayesian optimization of machine learning algorithms," in *Advances in neural information processing systems*, 2012, pp. 2951–2959.

[60] Y. Zhang, M. T. Bahadori, H. Su, and J. Sun, "Flash: fast bayesian optimization for data analytic pipelines," in *Proceedings of the 22nd ACM SIGKDD International Conference on Knowledge Discovery and Data Mining*, 2016, pp. 2065–2074.

[61] R. S. Olson, N. Bartley, R. J. Urbanowicz, and J. H. Moore, "Evaluation of a tree-based pipeline optimization tool for automating data science," in *Proceedings of the Genetic and Evolutionary Computation Conference 2016*, 2016, pp. 485–492.

[62] R. S. Olson and J. H. Moore, "Tpot: A tree-based pipeline optimization tool for automating machine learning," in *Workshop on Automatic Machine Learning*, 2016, pp. 66–74.

[63] R. S. Olson, R. J. Urbanowicz, P. C. Andrews, N. A. Lavender, J. H. Moore *et al.*, "Automating biomedical data science through tree-based pipeline optimization," in *European Conference on the Applications of Evolutionary Computation*, 2016, pp. 123–137.

[64] M. T. Ribeiro, S. Singh, and C. Guestrin, "Model-agnostic interpretability of machine learning," *arXiv preprint arXiv:1606.05386*, 2016.

[65] F. Doshi-Velez and B. Kim, "Towards a rigorous science of interpretable machine learning," 2017.

[66] P. W. Koh and P. Liang, "Understanding black-box predictions via influence functions," *arXiv preprint arXiv:1703.04730*, 2017.

[67] F. Hutter, H. H. Hoos, and K. Leyton-Brown, "Sequential model-based optimization for general algorithm configuration," in *International Conference on Learning and Intelligent Optimization*, 2011, pp. 507–523.

[68] J. S. Bergstra, R. Bardenet, Y. Bengio, and B. Kégl, "Algorithms for hyper-parameter optimization," in *Advances in neural information processing systems*, 2011, pp. 2546–2554.

[69] J. Močkus, "On bayesian methods for seeking the extremum," in *Optimization Techniques IFIP Technical Conference*, 1975, pp. 400–404.

[70] K. Eggensperger, M. Feurer, F. Hutter, J. Bergstra, J. Snoek, H. Hoos *et al.*, "Towards an empirical foundation for assessing bayesian optimization of hyperparameters," in *NIPS workshop on Bayesian Optimization in Theory and Practice*, 2013, vol. 10.

[71] L. Breiman, "Random forests," *Machine learning*, vol. 45, no. 1, pp. 5–32, 2001.

[72] C. Cortes and V. Vapnik, "Support-vector networks," *Machine learning*, vol. 20, no. 3, pp. 273–297, 1995.

[73] K. Simonyan and A. Zisserman, "Very deep convolutional networks for large-scale image recognition," *arXiv preprint arXiv:1409.1556*, 2014.

[74] C. Szegedy, V. Vanhoucke, S. Ioffe, J. Shlens, and Z. Wojna, "Rethinking the inception architecture for computer vision," in *Proceedings of the IEEE Conference on Computer Vision and Pattern Recognition*, 2016, pp. 2818–2826.

[75] J. B. Tenenbaum, V. De Silva, and J. C. Langford, "A global geometric framework for nonlinear dimensionality reduction," *science*, vol. 290, no. 5500, pp. 2319–2323, 2000.

[76] C. Bilgin, C. Demir, C. Nagi, and B. Yener, "Cell-graph mining for breast tissue modeling and classification," in *Engineering in Medicine and Biology Society, 2007. EMBS 2007. 29th Annual International Conference of the IEEE*, 2007, pp. 5311–5314.

[77] C. Gunduz, B. Yener, and S. H. Gultekin, "The cell graphs of cancer," *Bioinformatics*, vol. 20, no. suppl_1, pp. i145–i151, 2004.

[78] A. Chowdhury, E. Kautz, B. Yener, and D. Lewis, "Image driven machine learning methods for microstructure recognition," *Computational Materials Science*, vol. 123, pp. 176–187, 2016.

[79] H.-C. Shin, H. R. Roth, M. Gao, L. Lu, Z. Xu, I. Nogues *et al.*, "Deep convolutional neural networks for computer-aided detection: Cnn architectures, dataset characteristics and transfer learning," *IEEE transactions on medical imaging*, vol. 35, no. 5, pp. 1285–1298, 2016.